Electronic Supplementary Material (ESI) for ChemComm.

Supporting Information

An antioxidant boehmite amino-nanozymes able to disaggregate Huntington's inclusion bodies

Álvaro Martínez-Camarena,[a,*] Marian Merino,[b] Ana Virginia Sánchez-Sánchez,[b] Salvador Blasco,[a] José M. Llinares,[c] José L. Mullor,[b] Enrique García-España[a,*]

a) ICMol, Departamento de Química Inorgánica, University of Valencia, C/Catedrático José Beltrán 2, 46980, Paterna, Spain. E-mail: alvaro.martinez@uv.es ; enrique.garcia-es@uv.es

b) Bionos Biotech SL, Biopolo La Fe – IIS La Fe, Valencia, Spain. E-mail: jlmullor@iislafe.es

c) Departamento de Química Orgánica, University of Valencia, C/Dr Moliner s/n, 46100, Burjassot, Spain. E-mail: jollibe@uv.es

Content

SUMMARY OF FIGURES

Figure S14. Distribution diagram of (A) **L1** and (B) as a function of the pH in aqueous solution. The absorbance at 243 nm in the UV-Vis spectra is represented overlaid as diamonds (♦) for **L1**.

Figure S15. Spectra of a solution 10^{-3} M of **L1** at different pH values (from 2.04, depicted as pale orange, to 11.18, in dark orange).

Figure S16. Species distribution curves for the (A) Cu^{2+}:**L1** and (B) Cu^{2+}:**L2** systems in 0.15 M $NaClO_4$. The absorbance at 246 nm in the UV-Vis spectra is represented overlaid as diamonds (♦) for **L1**.

Figure S17. Spectra of a solution 10^{-3} M of Cu^{2+}:**L1** at different pH values (from 2.04, depicted as pale orange, to 11.18, in dark orange).

Figure S18. (A) Spectra of a solution 10^{-3} M of Cu(II):**L1** in 1:1 molar ratio, at different pH values (from 1.56, depicted as pale orange, to 3.88, in dark orange). (B) Representation of the absorbance at 730 nm in function of the pH of a solution 10^{-3} M of Cu(II):**L1** in 1:1 molar ratio.

Figure S19. Structure of the concatenated $[Cu(H_{-1}L1)]^+$ complexes. Top (A), lateral (B) and oblique (C) perspectives of the chain; only polar hydrogens have been represented for simplification. CCDC id. 2060436.

Figure S20. EPR measurement of a solution containing Cu(II):**L1** (blue line) or Cu(II):**L2** (orange) in 1:1 molar ratio. Baseline has been represented in grey.

Figure S21. ESI-HR-MS of Cu^{2+}-**L1** in H_2O.

Figure S22. Detail of the ESI-HR-MS spectrum of Cu^{2+}-**L1** in H_2O at *ca.* 350 g mol^{-1}. Both the experimental (in blue) and the theoretical (in red) spectra have been represented.

Figure S23. Detail of the ESI-HR-MS spectrum of Cu^{2+}-**L1** in H_2O at *ca.* 360 g mol^{-1}. Both the experimental (in blue) and the theoretical (in red) spectra have been represented.

Figure S24. Cyclic voltammograms at the glassy carbon electrode of a 1.0 mM solution of Cu^{2+}-**L1** (red) in 50 mM TRIS buffer at pH 7.0. Potential scan initiated at 0.2 V in the positive direction. Potential scan rate 50 mV s^{-1}. In blue and grey have been represented, respectively, the blank samples of 50 mM TRIS buffer and a 1 mM solution of **L1**.

Figure S25. Cyclic voltammograms at the glassy carbon electrode of a 1.0 mM solution of Cu^{2+}-**BNPL1** (red) in 50 mM TRIS buffer at pH 7.0. Potential scan initiated at 0.2 V in the positive direction. Potential scan rate 50 mV s^{-1}. In blue, grey and yellow have been represented, respectively, the blank samples of 50 mM TRIS buffer, a 1 mM solution of **L1** and a 0.1 M solution of $Cu(ClO_4)_2$ in the same conditions.

Figure S26. Fitting of the SOD activity data obtained by the McCord-Fridovich method for the system Cu-**L1**.

Figure S27. Fitting of the SOD activity data obtained by the McCord-Fridovich method for the system BNP-Cu-**L1**.

SUMMARY OF TABLES

I. MATERIALS AND METHODS

Potentiometric studies

Caution! Perchlorate salts are explosive and should be handled with care; such compounds should never be heated as solids. The potentiometric titrations were carried out at 298.1 ± 0.1 K using $NaClO_4$ 0.15 M as supporting electrolyte. The experimental procedure (burette, potentiometer, cell, stirrer, microcomputer etc.) has been fully described elsewhere.[5] The acquisition of raw potentiometric data was performed with the computer program PASAT.[6] The reference electrode was an Ag/AgCl electrode in saturated KCl solution. The glass electrode was calibrated as a hydrogen-ion concentration probe by titration of previously standardised amounts of HCl with CO_2-free NaOH solutions. The equivalent point was determined by Gran's method,[7,8] which gives the standard potential, E°, and the ionic product of water (pKw = 13.73(1)). The computer program HYPERQUAD was used to calculate the protonation and stability constants.[9] The HYSS[10] program was used to obtain the distribution diagrams. The pH range investigated using this technique was 2.5-11.0, in accordance with the linear response range of glass electrodes. When it was necessary to explore pH values below 2.5, due to the so called "acidic error", a correction was applied to the measured potential using the function:

$$E = E^o + s \cdot \log[H] + jp\,[H]$$

included in the VLpH program.[11] We have found for our working electrode E^o = 362.66 mV, s = 54.95 mV and jp = 48.40 mV · L · mol^{-1} and corrected the values accordingly before data treatment. The different titration curves for each system (at least two) were treated either as a single set or as separated curves without significant variations in the values of the stability constants. Finally, the sets of data were merged together and treated simultaneously to give the final stability constants.

NMR measurements

The ^1H and ^{13}C NMR spectra were recorded on a Bruker Advance DPX300 spectrometer operating at 300.13 MHz for ^1H and at 75.47 MHz for ^{13}C. For the ^1H spectra, the solvent signal was used as a reference standard. Adjustments to the desired pH values were made using drops of DCl or NaOD solutions. The pD was calculated from the measured pH values using the correlation, pH = pD - 0.4.[12]

UV-Vis measurements

The solvents used were of spectroscopic or equivalent grade. Water was twice distilled and passed through a Millipore apparatus. The pH values were measured with a Metrohm 713 pH-meter and adjustments of the hydrogen ion concentration of the solutions were made with diluted HCl and NaOH solutions. UV-Vis absorption spectra were recorded with an Agilent 8453 spectrometer.

Mass spectrometry measurements

The mass spectrometry analysis (ESI-MS and ESI-HR-MS) was carried out using an ESQUIRE 3000 PLUS Ion Trap Mass Spectrometer attached to an AGILENT 1100 (HPLC-MS) high-performance liquid chromatograph, coupled to an electro-spray ionization (ESI) source.

Dynamic light scattering determinations

The average size of the nanoparticles was determined by photon correlation microscopy, also known as dynamic light scattering. DLS was measured using a Malvern Mastersizer 2000 instrument. Solutions containing 1 mg of the NPs in 10 mL of a 1 x 10^{-4} M $NaClO_4$ aqueous solution at pH 7.4 were employed in the measurements.

ζ-Potential determination

The electric potential of the interfacial surface between the nanoparticles and the dispersion medium, also known as ζ-potential, was measured using a Malvern Mastersizer 2000 instrument. Solutions containing 1 mg of the NPs in 10 mL of a 1 x 10^{-4} M $NaClO_4$ aqueous solution at pH 7.4 were employed in the measurements.

Single crystal X-ray diffraction

Single-crystal X-ray diffraction (SXRD) data for the analysed structures were collected on a Xcalibur diffractometer (Agilent Technologies, Sapphire 3 CCD detector) using a single wavelength X-ray source with MoKα radiation, λ = 0.71073 Å and 120(1) K in all cases. The selected single crystals were mounted using Paratone-N hydrocarbon oil[13] on the top of a loop fixed on a goniometer head and immediately transferred to the diffractometer. Data collection, analytical absorption correction, and data reduction were performed with the Oxford program suite CrysAlisPro.[14] An empirical absorption correction was applied using spherical harmonics, implemented in SCALE3 ABSPACK scaling algorithm.[14]

The crystal structure was solved using direct methods with SHELXT,[15] and was refined by full-matrix least-squares methods on F^2 with SHELXL2014. All programs used during the crystal structure determination process are included in the OLEX2 software.[16] All the non-hydrogen atoms were anisotropically refined. Hydrogen atoms were introduced in calculated positions and their coordinates were refined according to a riding model, with the exception of the solvent water molecules. In some cases, analysis of the F map allowed localizing the water hydrogen atoms. CCDC 2060436 contains some of the supplementary crystallographic data, which can be obtained free of charge from The Cambridge Crystallographic Data Centre.[17] Table S1 contains additional information about the diffracted crystal and the corresponding measurements.

Table S1. Crystal data and structure refinement for [Cu(H$_{-1}$**L1**)]Cl.

	[Cu(H$_{-1}$**L1**)]Cl
Empirical formula	$C_{48}H_{68}Cl_4Cu_4N_{16}O_{24}$
Formula weight	1649.14
Temperature/K	120(1)
Crystal system	Orthorhombic
Space group	P ca2$_1$
a/Å	16.8069(4)
b/Å	17.5647(4)
c/Å	20.3780(5)
α/°	90
β/°	90
γ/°	90
Volume /Å^3	6015.8(2)
Z	4
d(calc) /g cm^{-3}	1.821
μ/mm^{-1}	1.670
F(000)	3373
2Θ range	2.62 to 66.0
Radiation /Å	0.71073
Refl. collected	84290
Independent refl.	22522
R_{int}	0.0692
restraints/param	19/866
GOF	1.014
R_1, wR_2[I>=2σ(I)]	R_1 = 0.0556 wR_2 = 0.1181
R_1, wR_2[all data]	R_1 = 0.1244 wR_2 = 0.1547
CCDC num.	2060436

Electrochemical Measurements

Cyclic voltammetric (CV) experiments were performed with 10^{-3} M aqueous solutions of **L1** and the functionalised nanoparticles at pH = 7.4. For the study of the electrochemistry of the metal complexes, 1 molar equivalent of $Cu(ClO_4)_2 \cdot 6H_2O$ and the ligand or the grafted nanoparticle were dissolved in 50 mM TRIS. Experiments combined air-saturated solution with progressively deaerated solutions by bubbling Ar. The experiments were carried out at 298 K using a glassy carbon working electrode (geometrical area 0.071 cm^2) in a conventional three-electrode cell completed with a Pt wire auxiliary electrode and a Ag/AgCl (3 M NaCl) reference electrode. A CH 660c potentiostatic device was used.

In vitro McCord-Fridovich SOD activity assays

The SOD-like activity was determined by using the nitro blue tetrazolium (NBT) method.[18–21] The assays were carried out in a pH = 7.4 50 mM HEPES buffer at 298 K. The xanthine (2.2×10^{-4} M) and xanthine oxidase system was used to generate a reproducible and constant flux of superoxide anions. The rate of reduction rate of NBT (7.3×10^{-5} M) to blue formazan was followed spectrophotometrically at 560 nm. Data in the absence of the complex were used as a reference. The rate of NBT reduction was progressively inhibited after the addition of the complex solutions at increasing concentrations prepared in 50 mM Tris-HCl buffer. The percentage of inhibition of the NBT reduction was used as a measure of the SOD activity of the compounds. The concentration of complex required to yield 50% inhibition of NBT reduction (IC_{50}) was determined from a plot of percentage inhibition versus complex concentration. The IC_{50} data have been calculated from the mean values of at least three independent measurements. The catalytic constant was calculated from the IC_{50} using the equation $k_{cat}=k_{NBT}[NBT]/IC_{50}$ where $k_{NBT}= (5.9 \pm 0.5) \times 10^5$ M^{-1} s^{-1}.[22–24]

Blank experiments were recorded with the ligands and/or the nanoparticles alone without observing any effect. Moreover, kinetics with the **BNP** + Cu^{2+} system were also carried out (in absence of **L1**), observing no significant difference with the catalytic activity of solutions of Cu^{2+} (without **BNP**).

Cell culture and transfection

Human embryonic kidney 293 cells (HEK293T) were cultured in DMEM high glucose medium, supplemented with penicillin-streptomycin and fetal bovine serum (Gibco, Fisher Scientific, Madrid, Spain). Cells were cultured into 75 cm^2 flasks at 37 °C with a 5% CO_2 humidified atmosphere. When cells reached 80% confluency, they were harvested with trypsin/EDTA (Gibco, Fisher Scientific, Madrid, Spain) and seeded at a density of 8×10^3 cells/mL into 96-well plates (Corning Incorporated, Kennebunk USA).

For generating a Huntington disease cell model to study antioxidant effects and reduction of protein aggregates, the transient expression of mutant huntingtin in HEK293T cells was induced. The cells were transfected with Lipofectamine™ 3000 (Invitrogen, Fisher Scientific, Madrid, Spain) according to manufacturer's recommendations, with a plasmid containing huntingtin exon 1 protein with a polyQ stretch of 121 glutamines, with the CMV promoter and the red fluorescent protein mCherry. After the transfection, cells were incubated 24 h under standard conditions in medium containing 5 μM or 0.1 μM of each compound to study their effects.

MTT assay

To determine cell viability, 3-(4,5-dimethylthiazol-2-yl)-2,5-diphenyltetrazolium bromide (Sigma Aldrich, Darmstadt, Germany) was used. HEK293T cells were treated with the studied compounds or with growth medium (controls) for 24 h. After that, cells were incubated with the MTT reagent for 3 h and dimethyl sulfoxide (Sigma Aldrich, Darmstadt, Germany) was used to dissolve the formazan product. The resulted color intensity was measured at 550 nm in a spectrophotometer Halo LED 96 (Dynamica Scientific, Livingston, UK). Blank experiments to determine the toxicity of the non-functionalized BNPs and the systems employed as reference have also been carried out.

Mitochondrial superoxide detection (MitoROS)

To detect the intracellular superoxide radicals in HEK293T cells expressing mutant huntingtin, the Mitochondrial Superoxide Detection kit (Fluorometric) (Abcam, Cambridge, UK) was used. Cells were transfected in order to express the mutant huntingtin and generate oxidative stress. After that, cells were treated for 24 h and processed according to manufacturer's instructions.

The background signal was measured due to a possible interference of mutant huntingtin with the red fluorescent protein mCherry and the mitoROS reagent (see Figure S1), the emitted fluorescence of transfected cells without the mitoROS reagent was at control cells level. In other words, the red signal of the mHTT was not generating any background. Then, when mitoROS reagent was added to the cells, the signal highly increased in the cells expressing mutant huntingtin, meaning that mitochondrial oxidative damage was being generated due to the impaired protein and its toxicity.

Blank experiments to determine the activity of the non-functionalized BNPs and the systems employed as reference have also been carried out. The blank assays (Figure S2) show that neither the non-functionalized nanoparticles nor the reference compound **L2** or a mixture of non-grafted ligand, Cu^{2+} and NPs present any significant activity.

For testing the ability of our compounds in reducing the superoxide anion produced in the mitochondria, HEK293T cells were treated during 24 h with each compound at 5 μM, except for **BNP-L1**, Cu^{2+}:**BNP-L1**, **BNP-L4** and Cu^{2+}:**BNP-L4**, that 0.1 μM was chosen.

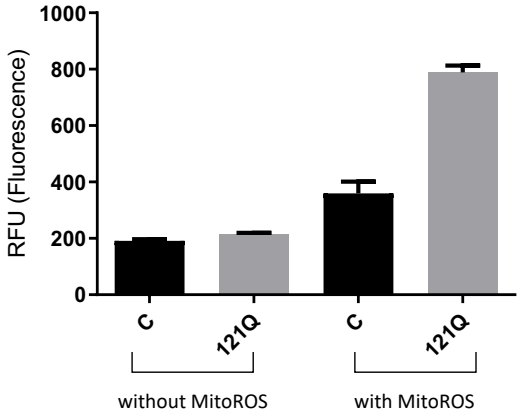

Figure S1. Representation of the fluorescence of transfected cells with and without generation of mitoROS.

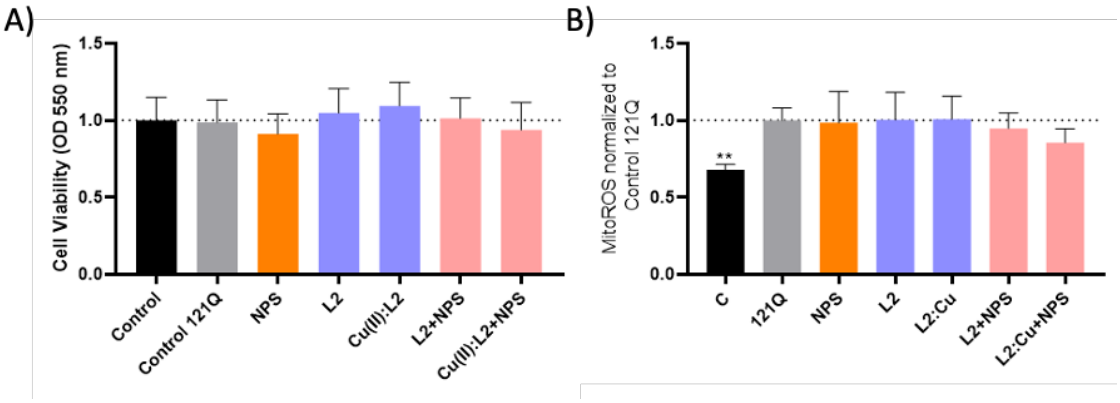

Figure S2. Results of the blank experiments. Representation of the results of (A) the cell viability of HEK293T cells and (B) the fluorescence of transfected cells in presence of non-functionalized BNPs, **L2** and Cu(II)-**L2** and of mixtures of **L2**+BNPs and Cu(II)-**L2**+BNPs. All the solutions tested are 5 μM.

Protein aggregates determination

To test whether these compounds could help in reducing protein aggregates, we evaluated such activity in cells expressing mHTT. HEK293T cells were transfected with a plasmid encoding the protein corresponding to exon 1 of the HTT gene with an elongated polyglutamine region of 121 CAG. Additionally, this region contained the red fluorescent protein mCherry, in order to be able to visualize the protein aggregates to the microscope.

After the transfection, cells were incubated 24 h in medium (control) or medium containing 5 μM or 0.1 μM of each compound. Following that, cells were processed for

microscope analysis. First, cells were fixed with paraformaldehyde 2% (Electron Microscopy Sciences, Hatfield, Pennsylvania, USA) in DMEM medium for 15 minutes. Then, they were stained with DAPI and Phalloidin 488 (Sigma Aldrich, St. Louis, Missouri, USA) for 30 min to identify individual cells and be able to calculate the percentage of cells containing red fluorescent aggregates (see Figure S3). After that, cells were washed and kept in PBS (Gibco, Sigma Aldrich, St. Louis, Missouri, USA) for image analysis. Measurements were carried out with the In Cell Analyzer 2000 (GE Healthcare Life Sciences, Chicago, USA), whilst the In Cell Investigator Image Analysis Software was employed to determine the percentage of cells with huntingtin aggregates (positive cells) and the percentage of cells that do not present protein aggregates (negative cells).

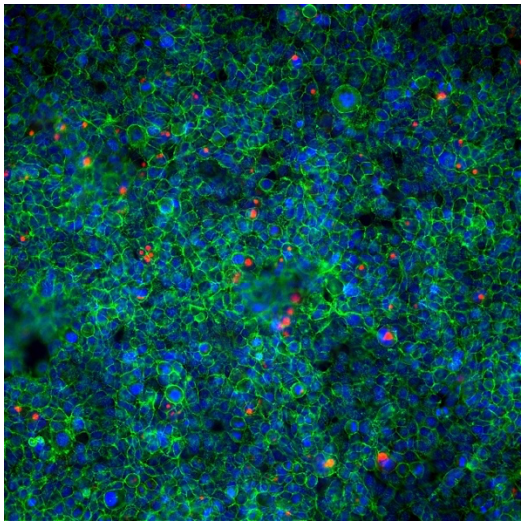

Figure S3. Example of the visualization in the microscope of the treated cells.

Statistical analysis

The statistical analysis was performed with GraphPad Prism software, version 6 (GraphPad, San Diego, CA, USA). Data are represented as mean ± SEM and the test applied for the analysis was the ordinary one-way ANOVA test with Dunnet post-Hoc and unpaired Student's t-test. Statistical significance was set at $p < 0.05$, 95% of confidence.

II. SYNTHESIS AND CHARACTERISATION

All reagents were obtained from commercial sources and used as received. Solvents used for the chemical synthesis were of analytical grade and used without further purification. A detailed scheme of the synthesis can be found in Figure S4, while further details of the characterization of **L1** and **BNP-L1** are located in Figures S5 – S13.

Synthesis of L1

*Synthesis of methyl 2,6-bis(hydroxymethyl)isonicotinate (**2**).*[25–27] Methyl isonicotinate (**1**, 0.55 g, 4.01 mmol) was dissolved in 20 mL of methanol and the solution was acidified with concentrated H_2SO_4 (50 µL, 0.94 mmol). Then, the mixture was heated under reflux. Once the suspension reached the boiling temperature, ammonium peroxydisulfate (9.01 g, 39.48 mmol) in 20 mL of water was added dropwise. After 1 hour at reflux, the reaction mixture was cooled down and then concentrated under reduced pressure. The mixture was neutralized using a saturated aqueous solution of $NaHCO_3$ and then extracted with CH_2Cl_2 (3 x 50 mL). The organic phases were combined and dried with anhydrous Na_2SO_4. Finally, the solid was filtered off and the solvent evaporated to dryness under

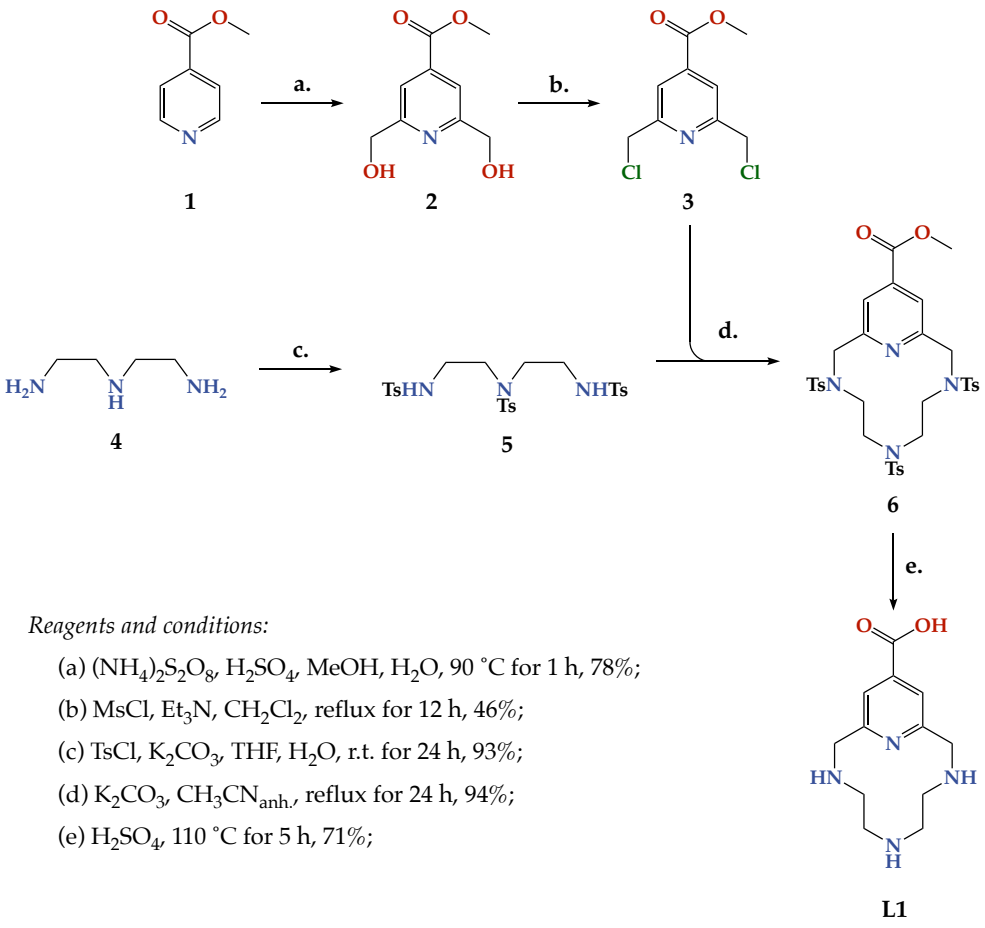

Figure S4. Synthetic route for the preparation of the polyaza-macrocyclic receptor **L1**, from methyl isonicotinate and diethylenetriamine.

reduced pressure to obtain the pure product as a yellow solid (0.62 g, 78 %). ^{1}H NMR (300.1 MHz, DMSO-d6), δ (ppm): 7.80 (s, 2H), 5.58 (t, J = 5.9 Hz, 2H), 4.62 (d, J = 5.9 Hz, 4H), 3.92 (s, 3H). ^{13}C NMR (75.5 MHz, DMSO-d6), δ (ppm): 166.0, 163.2, 138.3, 117.4, 64.3, 53.2.

*Synthesis of methyl 2,6-bis(chloromethyl)isonicotinate (**3**).*[28] Compound **2** (1.10 g, 5.58 mmol) was suspended in dichloromethane (60 mL) and triethylamine (1.85 mL, 13.39 mmol) and mesyl chloride (1.04 mL, 13.39 mmol) were added. After stirring overnight at reflux, the acidic solution was neutralized with a saturated solution of $NaHCO_3$ (50 mL) and the resulting mixture was extracted with CH_2Cl_2 (3 x 60 mL). The combined organic phases were dried with anhydrous Na_2SO_4, the solid was filtered and the solvent evaporated to dryness under reduced pressure. Compound **3** was obtained as a white solid (0.60 g, 46 %). ^{1}H NMR (300.1 MHz, $CDCl_3$), δ (ppm): 7.95 (s, 2H), 4.68 (s, 4H), 3.94 (s, 3H). ^{13}C NMR (75.5 MHz, $CDCl_3$), δ (ppm): 164.8, 157.6, 139.8, 121.5, 52.9, 46.0.

*Synthesis of 1,4,7-tris(ρ-tolylsulfonyl)-1,4,7-triazaheptane (**5**).* The polyamine **4** (1.55 g, 15.00 mmol) was dissolved in 200 mL of THF and the resulting solution was merged with 50 mL of K_2CO_3 (7.26 g, 52.50 mmol) in water. A solution of *p*-tolylsulfonyl chloride (10.01 g, 52.50 mmol) in 50 mL of THF was then added under intense stirring. The reaction mixture was kept for 24 h and then the organic solvent was evaporated under reduced pressure. The resulting aqueous solution was extracted with CH_2Cl_2 (3 x 50 mL) and the combined organic phases were dried with anhydrous Na_2SO_4. The solid was filtered and the solvent evaporated to dryness under reduced pressure. The residue was suspended in ethanol and heated under reflux for 2 h, obtaining a white solid that was filtered and washed with ethanol (7.90 g, 93%). ^{1}H NMR (300.1 MHz, $CDCl_3$), δ (ppm): 7.76 (d, *J* = 8.3 Hz, 4H), 7.61 (d, *J* = 8.3 Hz, 2H), 7.31 (d, *J* = 7.8 Hz, 4H), 7.30 (d, *J* = 8.4 Hz, 2H), 5.30 (s, 2H), 3.22 – 3.08 (m, 8H), 2.43 (s, 9H). ^{13}C NMR (75.5 MHz, $CDCl_3$), δ (ppm): 143.6, 136.6, 130.0, 129.8, 127.3, 127.2, 50.5, 42.6, 21.6.

*Synthesis of methyl 3,6,9-tris(ρ-tolylsulfonyl)-3,6,9-triaza-1(2,6)-pyridinecyclodecaphane-1^{4}-carboxylate (**6**).* The tosylated polyamine **5** (1.61g, 2.85 mmol) and K_2CO_3 (2.36 g, 17.09 mmol) were suspended in anhydrous acetonitrile (150 mL) and the resulting mixture was stirred and heated to reflux. Then, compound **3** (0.8 g, 3.42 mmol) was dissolved in 50 mL of anhydrous acetonitrile and the resulting solution was added dropwise very slowly (with a rate of *ca.* 20 mL/h) over the first suspension. The mixture was kept at reflux under an inert atmosphere for 24 h. Once the reaction time had elapsed, it was cooled down and the solid was filtered off. The solvent of the resulting solution was evaporated under reduced pressure. Compound **6** was purified by washing and stirring the impure oil in warm methanol, keeping the resulting mixture at reflux. After 4 h, the

suspension was filtered off and the solid was washed with cold methanol (1.95 g, 94%). ^{1}H NMR (300.1 MHz, $CDCl_3$), δ (ppm): 7.94 (s, 2H), 7.72 (d, *J* = 8.3 Hz, 4H), 7.66 (d, *J* = 8.3 Hz, 2H), 7.35 (d, *J* = 8.3 Hz, 4H), 7.28 (d, *J* = 8.2 Hz, 2H), 4.36 (s, 4H), 3.96 (s, 3H), 3.32 (t, *J* = 7.5 Hz, 4H), 2.98 – 2.76 (m, 4H), 2.45 (s, 6H), 2.41 (s, 3H). ^{13}C NMR (75.5 MHz, $CDCl_3$), δ (ppm): 164.6, 156.7, 143.9, 143.6, 140.5, 135.9, 135.1, 130.0, 129.8, 127.2, 127.1, 123.4, 54.9, 53.0, 50.2, 47.7, 21.6, 21.5. MS *m*/*z* (ESI) 727.2 g mol^{-1} ([M+H]$^{+}$).

*Synthesis of 3,6,9-triaza-1(2,6)-pyridinecyclodecaphane-1^{4}-carboxylic acid (**L1**·HSO_4·$(HCl)_{2.4}$).*[29] Compound **6** (0.50 g, 0.69 mmol) was dissolved in H_2SO_4 (10 mL, 0.19 mol) and the resulting solution was stirred at 110 ˚C for 5 h. After cooling, the mixture was added dropwise over 100 mL of dry ethanol. The product was precipitated as a salt by the addition of 100 mL of diethyl ether to the ethanolic solution. Finally, the suspension was filtered and washed several times with anhydrous EtOH. In order to obtain the pure acid compound, the precipited salt was dissolved in 20 mL of Milli-Q water in presence of 25 μL of HCl and the resulting solution was refluxed for 24 h. The solvent was evaporated under reduced pressure to obtain the hydrolysed compound as a pale brown salt (0.27 g, 71%). Complete details of the characterization of the compound are provided in Figures S5-S8.

^{1}H NMR (300.1 MHz, D_2O), δ (ppm): 7.94 (s, 2H), 4.76 (s, 4H), 3.73 – 3.66 (m, 4H), 3.65 – 3.58 (m, 4H). ^{13}C NMR (75.5 MHz, D_2O), δ (ppm): 167.1, 151.7, 141.0, 122.3, 49.7, 44.0, 42.3. MS *m*/*z* (ESI) 251.0 g mol^{-1} ([M+H]$^{+}$). Anal. Calcd. for $C_{12}H_{18}O_2N_4$·HSO_4·$(HCl)_{2.4}$: C, 32.6; H, 5.1; N, 12.7: Found: C, 32.7; H, 5.5; N, 12.6.

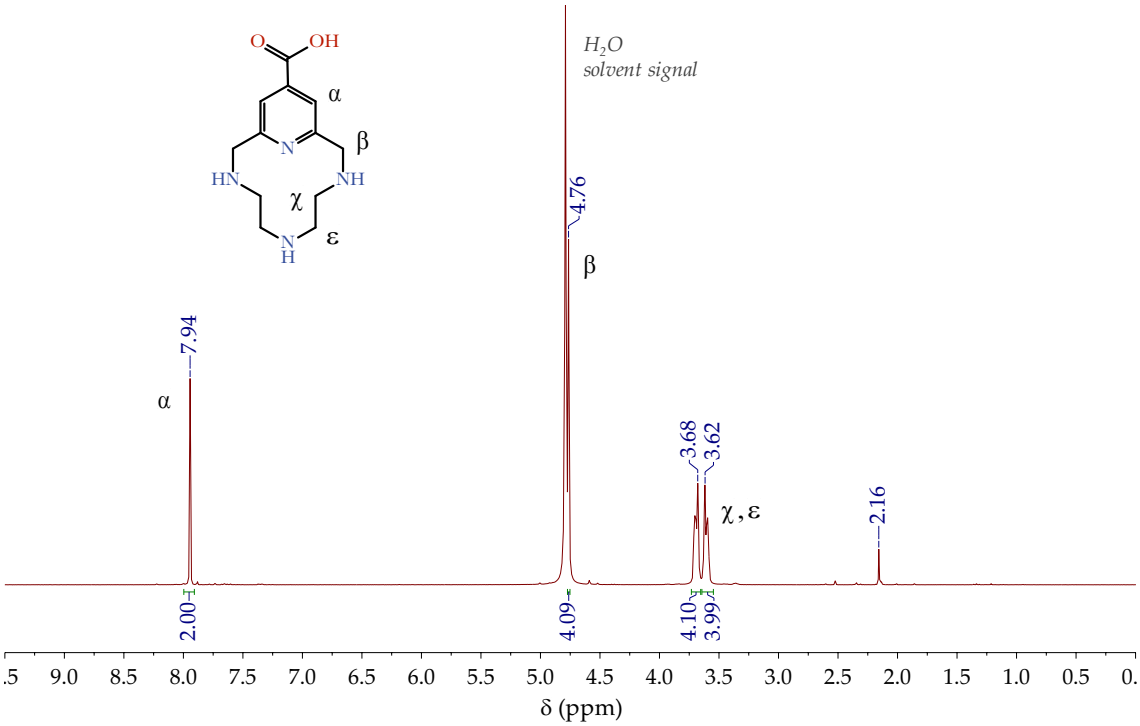

Figure S5. ^{1}H-NMR spectrum of **L1** in D_2O at 298 K.

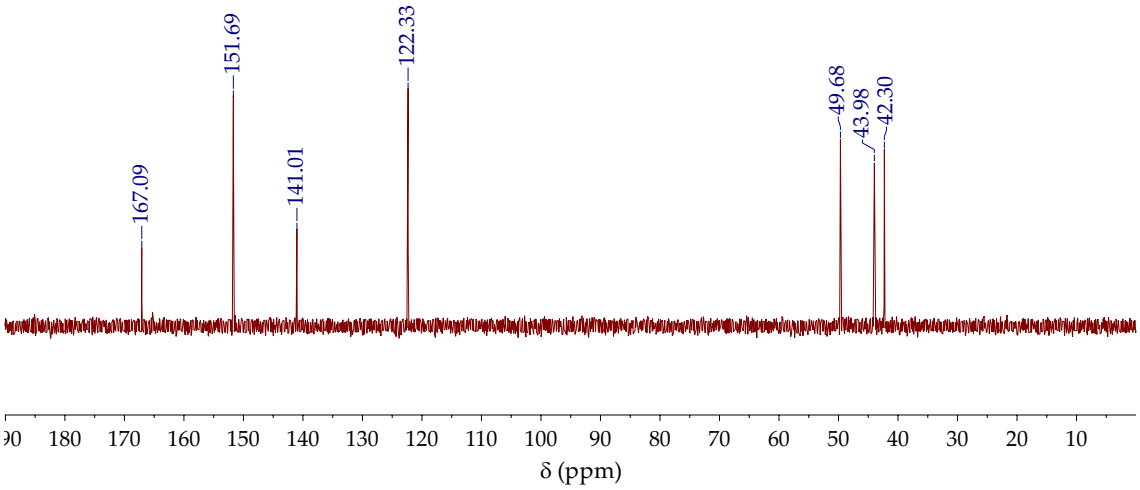

Figure S6. ^{13}C-NMR spectrum of **L1** in D_2O at 298 K.

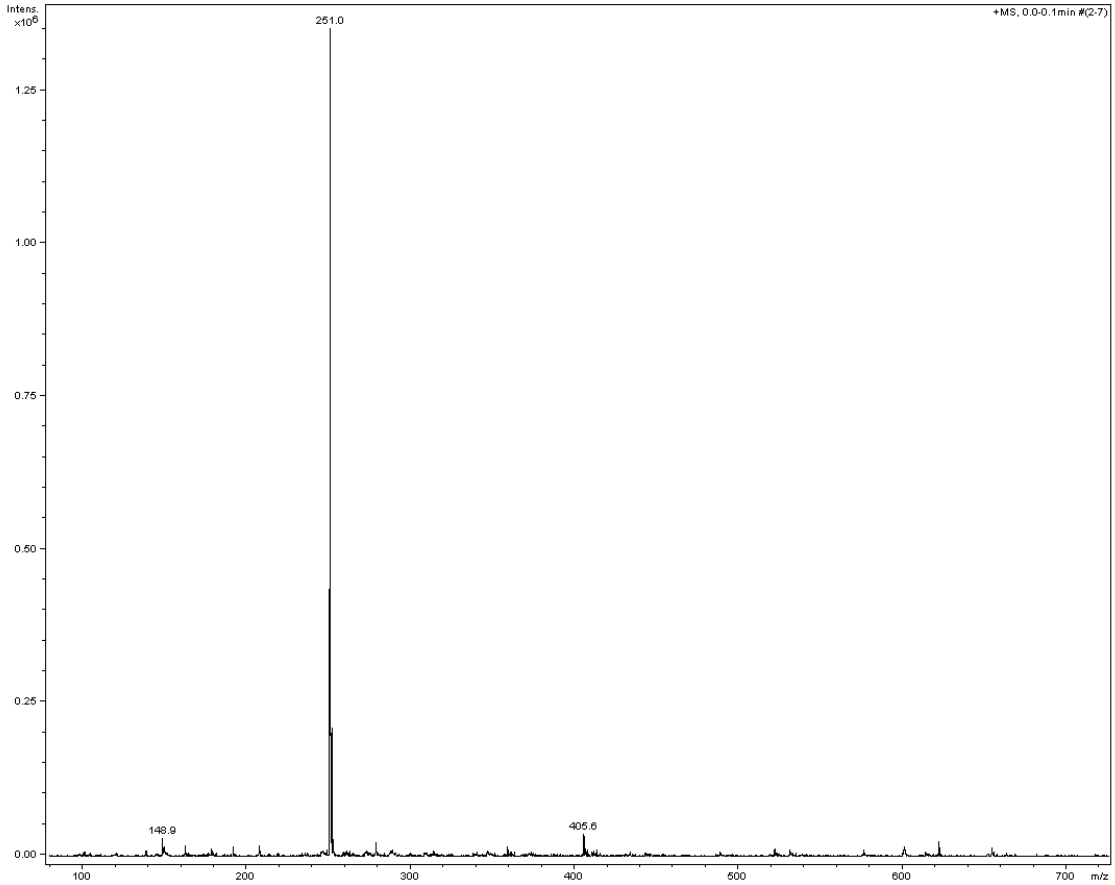

Figure S7. LC-MS (ESI/APCI-TOF) of **L1** in H_2O.

Synthesis of the boehmite nanoparticles

Boehmite nanoparticles (BNPs) were prepared by a two-step procedure already described.[30] To synthesize the BNPs, 146 mL of Milli-Q water were heated to 80 ˚C for an hour and then the aluminium tert-butoxide (20.00 g, 81.2 mmol) was added, increasing the suspension temperature to 85 ˚C. One hour after, the reaction mixture was completed with the addition of 1.12 mL of HNO_3. The resulting mixture was stirred for 5 days at 95 ˚C and then the solvent was removed by evaporation under reduced pressure. The solid was dried at 120 ˚C for 24 h, powdered and washed with an EtOH:H_2O 90:10 vol/vol mixture.

The X-ray diffraction pattern presents peaks at 14.60, 28.10, 38.10, 48.90, 55.20, 64.10, 65.10 and 72.00 values of 2θ˚, characteristics of the crystalline structure of γ-boehmite. As shown in Figure S8, the experimental X-ray powder diffraction pattern matches the theoretical spectrum. On the other hand, the DLS (Figure S9) studies show an average nanoparticle diameter of *ca.* 58 nm. It can also be found a small portion of particles with a size smaller than 10 nm as well as a small group of agglomerates that present particle diameters bigger than 100 nm.

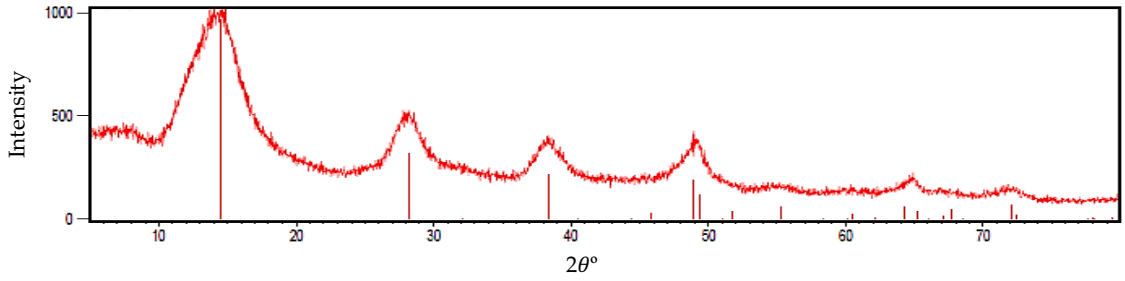

Figure S8. Experimental (red, continuous line) and theoretical (discrete red peaks) diffractogram of the boehmite nanoparticles powder.

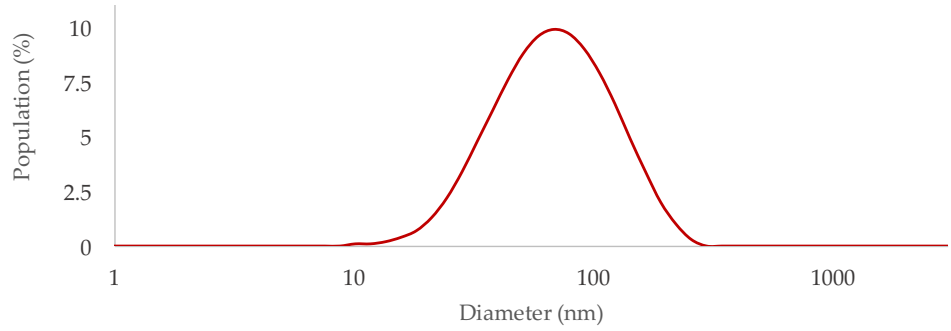

Figure S9. Size dispersion diagram of the boehmite nanoparticles obtained by DLS.

Functionalization of the boehmite nanoparticles

The grafting of the azamacrocyclic ligand to the BNPs was carried out through a nucleophilic attack to its carbonyl group and the formation of the corresponding amide group (see Figure S10). In order to have an effective nucleophilic attack, it was necessary the previous functionalization of the boehmite surface with (3-aminopropyl)triethoxysilane. Therefore, the functionalization of the ligand was performed in two successive steps: (I) the grafting of the silane compound to the boehmite surface and (II) the binding of the azamacrocyclic ligand to the functionalised intermediate.[31,32]

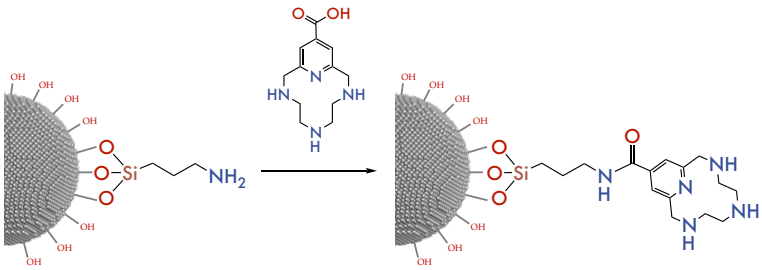

Figure S10. Synthetic route for the grafting of the ligands onto the surface of the boehmite nanoparticles. *Reagents and conditions:* (3-aminopropyl)triethoxysilane, EtOH, r.t. for 48 h; then L1, HCl, EtOH, reflux for 20 h.

To carry out the silane functionalization, 0.7 mL (2.99 mmol) of (3-aminopropyl)triethoxysilane and 488 mg of boehmite nanoparticles were suspended in 14 mL of dry ethanol. The suspension was refluxed under an Ar/N_2 atmosphere for 48 h and then, it was centrifuged and washed several times with a mixture of EtOH (15 mL), CH_2Cl_2 (5 mL) and H_2O (2.5 mL).

Once the nanoparticles were functionalised with the silane-propylamine moieties, 170 mg of them were re-suspended in 8 mL of EtOH containing the ligand (0.65 mmol) and 50 μL of conc. HCl. The reaction mixture was refluxed for 20 h under an Ar atmosphere and the suspension was then centrifuged and washed several times with a mixture of EtOH (15 mL), CH_2Cl_2 (5 mL) and H_2O (2.5 mL).

The ligand and the Cu^{2+} content of the material were quantified by ^{1}H NMR spectroscopy and ICP-MS analysis, respectively. In the first case, a series of solutions containing **L1** with concentrations from $2x10^{-4}$ to $4x10^{-3}$ M in D_2O were measured by ^{1}H NMR spectroscopy at pH *ca.* 3 (to maximize the solubility of the nanoparticles). The area of each proton signal was integrated and normalized with respect to the TMS signal employed as an internal standard. The resulting calibration plot was used to interpolate the integration areas of solutions containing different amounts of functionalized nanoparticles (5 ~ 10 mg in 1 mL of D_2O) at pH *ca.* 3. The NMR spectra of the functionalised NPs as well as the calibration fittings can be found in Figures S11 and S12.

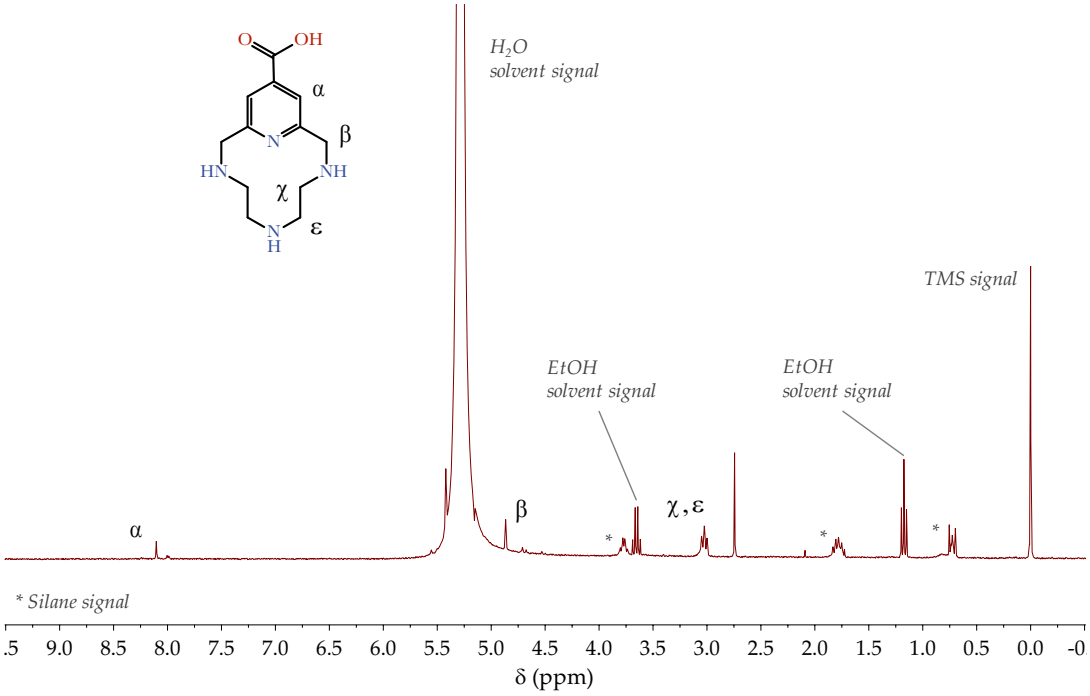

Figure S11. ^{1}H-NMR spectrum of a **BNP-L1** sample in D_2O at 298 K.

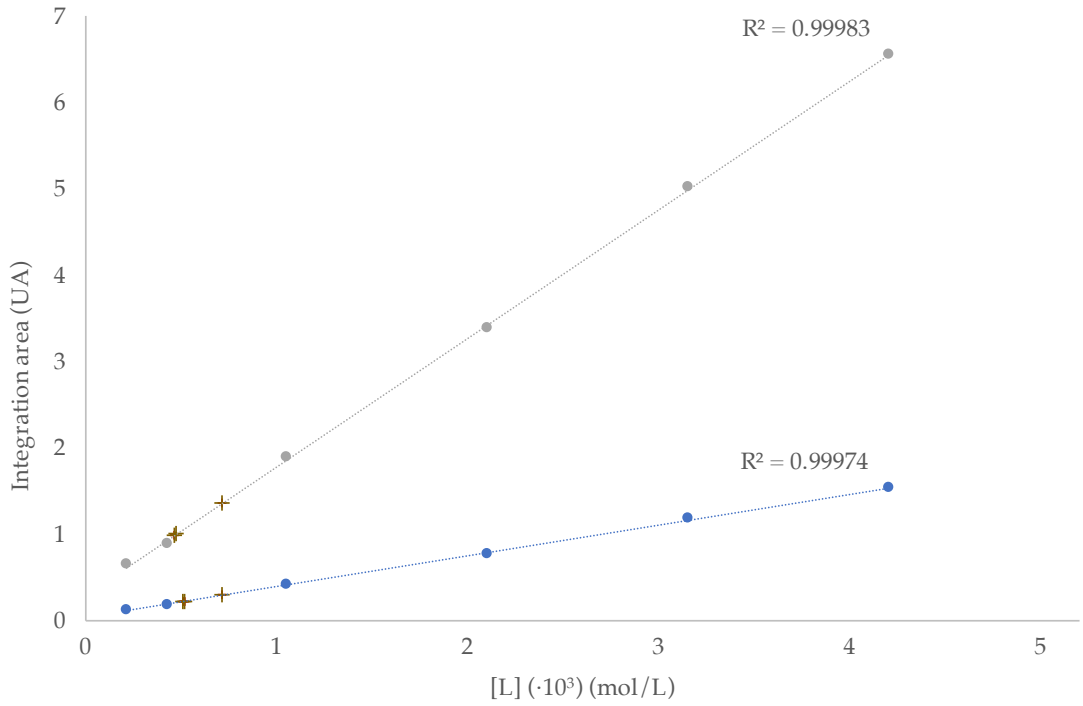

Figure S12. Calibration and interpolation of **L1** anchoring to boehmite nanoparticles by NMR determination.

On the other hand, ICP-MS analysis was used to quantify the amount of Cu^{2+} that the grafted nanoparticles were able to chelate, as well as to elucidate if metal ion release

takes place as a function of time (in short periods of time). For this, 15~25 mg of functionalized NPs were suspended in ca. 2 mL of Milli-Q water. The pH of the resulting suspensions was adjusted to 7.4. Then, a Cu^{2+}solution was added to the suspension and the resulting mixture was stirred for 30 min. The mixture was centrifuged. The solid residue (corresponding to the nanoparticles) was then washed several times with Milli-Q water at pH 7.4, centrifuging after each washing and discarding the resulting solution. Finally, the grafted nanoparticles were resuspended in 2 mL of Milli-Q water at pH *ca.* 1 to release the chelated Cu^{2+}, and the suspension was centrifuged one last time. The resulting solution, that contains the total amount of Cu^{2+} coordinated by the functionalized BNPs, was studied by means of ICP-MS. According to the results of the ^{1}H NMR and the ICP-MS analysis, the amount of **L1** onto the BNP is $1.03(5)\cdot10^{-4}$ mol/gNP, and the grafted NPs are able to coordinate $0.79(6)\cdot10^{-4}$ mol Cu^{2+}/g_{NP}.

Table S2. Concentration of the grafted ligand and ζ-potential values determined for the different systems of nanoparticles. All measurements were carried out in 10^{-4} M $NaClO_4$ at pH 7.4.

System	[L] (mol/g_{NP})	ζ-potential (mV)
BNP	-	32.1(8)*
BNP-L1	$1.03(5)\cdot10^{-4}$	16.1(6)

* Values in parenthesis are standard deviations in the last significant figure.

Finally, the ζ-potential of both the functionalised and the non-functionalised, oxidic nanoparticles was determined. The obtained values can also be found in Table S2 and Figure S13. Functionalization of the nanoparticles with the macrocycles causes a slight modification of their surface potential maintaining, in general terms, the positive sign of the charge.

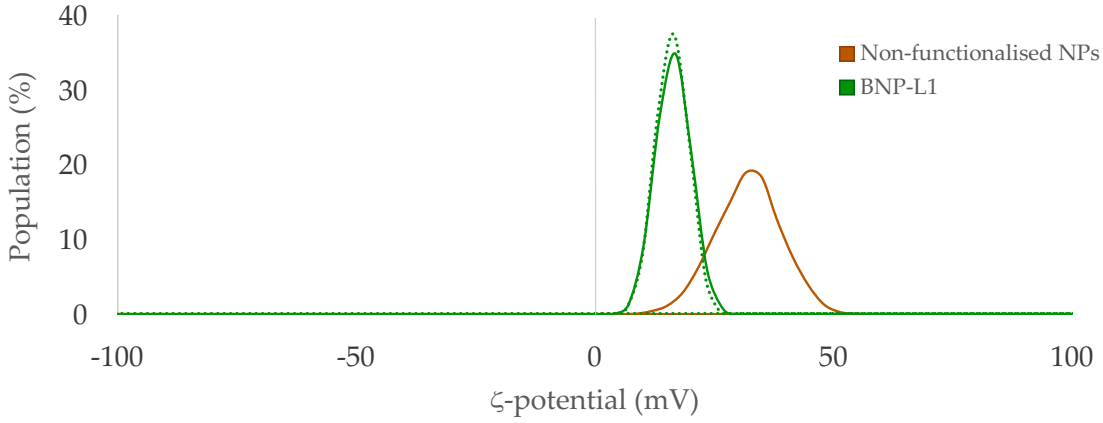

Figure S13. Experimental ζ-potential of the oxidic nanoparticles. The continuous lines correspond to solutions of nanozymes in absence of Cu^{2+}, while the dotted ones correspond to solutions of nanozymes in presence of Cu^{2+}, in Cu^{2+}-**L1** 1:1 molar ratio.

III. BEHAVIOUR IN SOLUTION

Acid-base behaviour

The protonation constants of the azamacrocycle obtained by potentiometric titrations are shown in Table S3. The distribution diagram as a function of the pH can be found in Figure S14.

Table S3. Logarithms of the stepwise protonation constants for **L1** and **L2**[1] obtained by potentiometric studies. The constants were determined in 0.15 M $NaClO_4$ at 298.1 ± 0.1 K. . $H_{-1}L$ corresponds with the form of **L1** in which the carboxylic acid is deprotonated.

Reaction	L1
$H_{-1}L^- + H^+ \rightleftarrows H(H_{-1}L)$	10.80(1)[a]
$(H_{-1}L) + H^+ \rightleftarrows H_2(H_{-1}L)^+$	7.90(1)
$H_2(H_{-1}L)^+ + H^+ \rightleftarrows H_2L^{2+}$	2.25(2)

[a] Values in parentheses are standard deviations in the last significant figure.

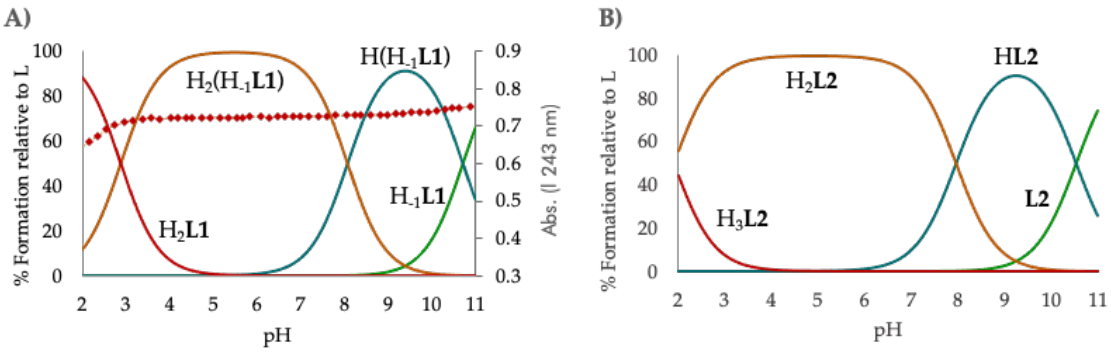

Figure S14. Distribution diagram of (A) **L1** and (B) as a function of the pH in aqueous solution. The absorbance at 243 nm in the UV-Vis spectra is represented overlaid as diamonds (♦) for **L1**.

The two first constants are rather hight, particularly the first one, in comparison with the basicity constants of secondary and tertiary amines reported in the bibliography, which usually are *ca.* 9-10 logarithmic units.[38] In agreement with related macrocyclic polyamines, the extra stability of the protonated systems can be explained by the formation of internal hydrogen bonds within the macrocyclic structures.[1] Therefore, we can assume that the first two protonation reactions involve amino groups of the macrocycle. This conclusion is also consistent with the UV spectra since there is not any significant change in the absorption band of the pyridine as the pH decreases from 11 to

4, that is, in correspondence with the first and the second protonation steps (see Figures S14 and S15). The third protonation step involves the carboxylate group, as supported by the UV spectroscopy studies since the absorbance of the pyridine unit at 243 nm decreases significantly from pH 4 to 2, in correspondence with the third protonation (see Figure S14).[1,39]

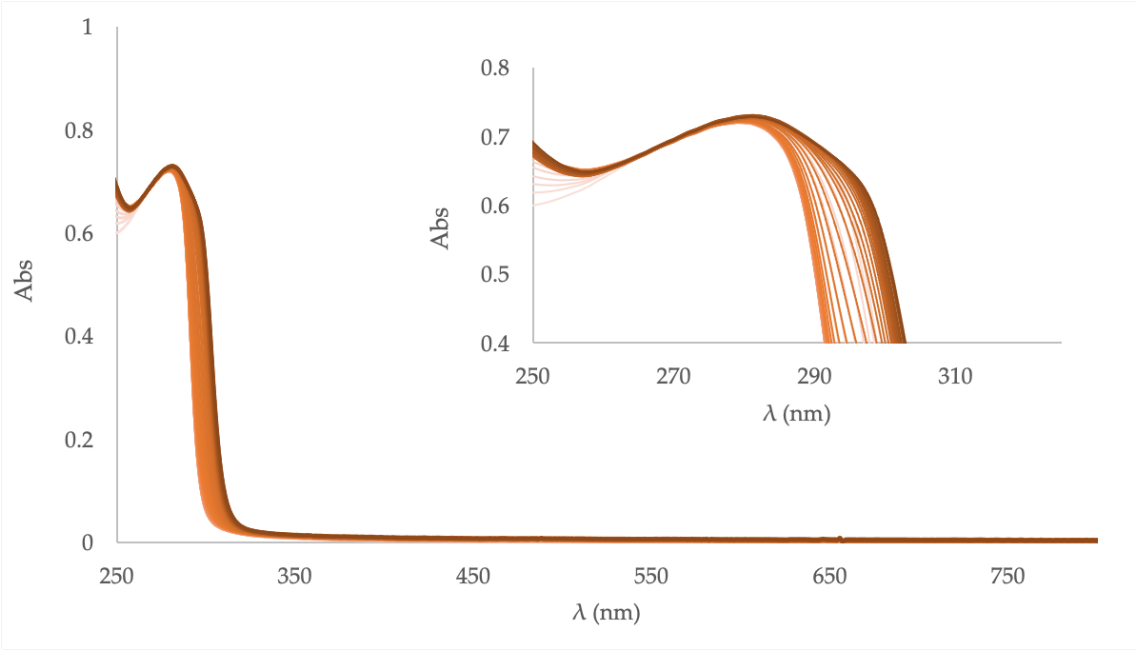

Figure S15. Spectra of a solution 10^{-3} M of **L1** at different pH values (from 2.04, depicted as pale orange, to 11.18, in dark orange).

Interaction with Cu^{2+}

The interaction of Cu^{2+} with **L1** has been studied by pH-metric titrations, UV-Vis spectroscopy, high resolution mass spectrometry, EPR and X-ray diffraction methods. The stability constants obtained are shown in Table S4. The representation of the distribution diagrams as a function of the pH can be found in Figures S16. The UV-vis measurements can be found in Figures S17 and S18.

Table S4. Logarithms of the stepwise stability constants for the Cu^{2+} complexes of **L1** and **L2**[1] obtained by potentiometric measurements. The constants were determined in 0.15 M $NaClO_4$ at 298.1 ± 0.1 K. $H_{-1}L$ corresponds with the form of **L1** in which the carboxylic acid is deprotonated.

Reaction	L1
$Cu^{2+} + H_{-1}L^{-} \rightleftarrows [Cu(H_{-1}L)]^{+}$	17.62(2)[a]
$[Cu(H_{-1}L)]^{+} + H_2O \rightleftarrows [Cu(H_{-1}L)(OH)] + H^{+}$	-9.07(2)

[a] Values in parentheses are standard deviations in the last significant figure.

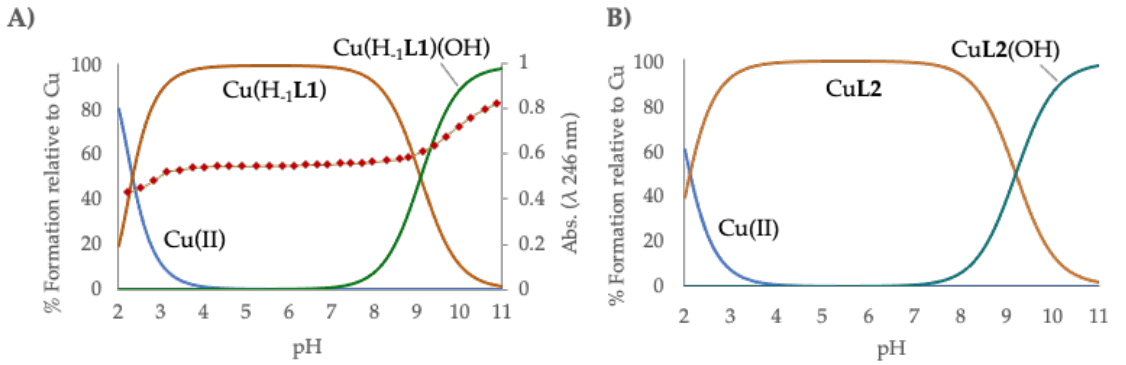

Figure S16. Species distribution curves for the (A) Cu^{2+}:**L1** and (B) Cu^{2+}:**L2** systems in 0.15 M $NaClO_4$. The absorbance at 246 nm in the UV-Vis spectra is represented overlaid as diamonds (♦) for **L1**.

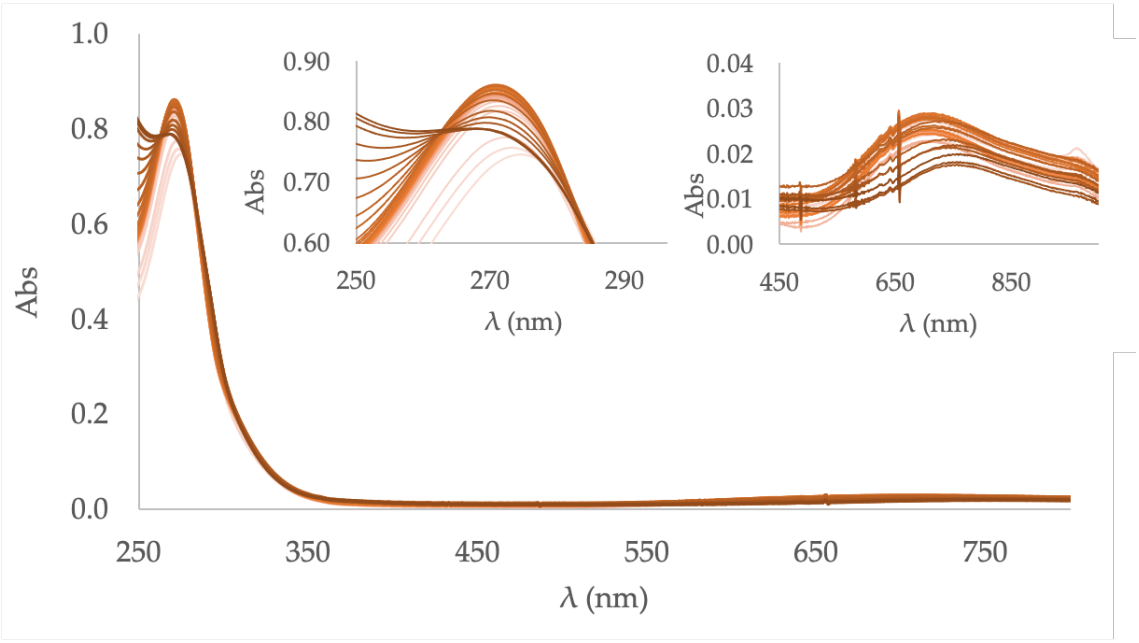

Figure S17. Spectra of a solution 10^{-3} M of Cu^{2+}:**L1** at different pH values (from 2.04, depicted as pale orange, to 11.18, in dark orange).

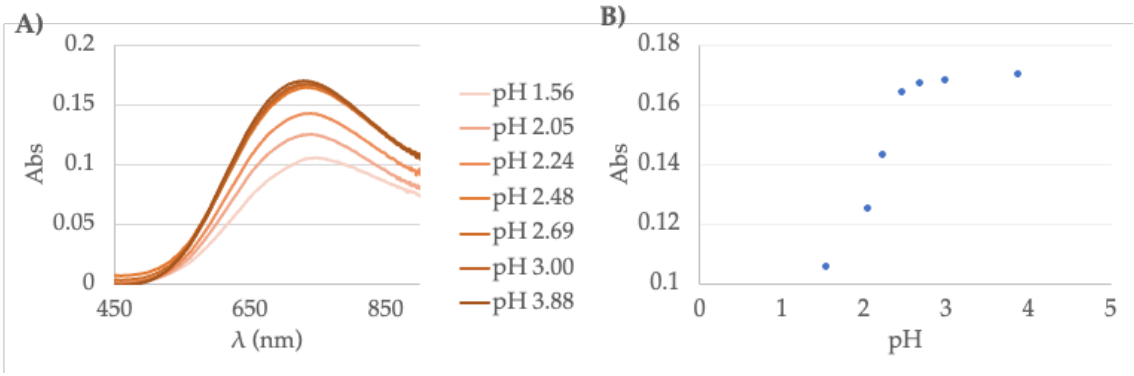

Figure S18. (A) Spectra of a solution 10^{-3} M of Cu(II):**L1** in 1:1 molar ratio, at different pH values (from 1.56, depicted as pale orange, to 3.88, in dark orange). (B) Representation of the absorbance at 730 nm in function of the pH of a solution 10^{-3} M of Cu(II):**L1** in 1:1 molar ratio.

The speciation of the Cu^{2+}:**L1** system is quite simple, with the formation of the mononuclear $[Cu(H_{-1}\mathbf{L1})]^{+}$ and $[Cu(H_{-1}\mathbf{L1})(OH)]$ complexes. The value of the stability constant of the mononuclear, unprotonated complex is a little lower than the one some of us reported for **L2**, the macrocycle with the unsubstituted pyridine ring (**L2**).[1] This can be attributed to the withdrawing effect of the carboxylate group. Nevertheless, the differences in the stability of the complexes might be somehow counterbalanced by the negative charge of **L1**. The EPR spectra support the formation of axially distorted Cu^{2+} complexes.

A crystalline sample of the Cu^{2+}-**L1** system was obtained by slow evaporation of aqueous solution containing $Cu(ClO_4)_2{\cdot}6H_2O$ and **L1** at pH = 6 (see Figure S19). The crystals show the formation of chains in which the complex $[Cu(H_{-1}\mathbf{L1})]^{+}$ can be identified as the fundamental monomer. In such polymers, concatenation takes place through the interaction of the copper atom of one complex (by its fourth equatorial position), with one oxygen of the carboxylate group of the next monomer, as seen in Figure S19. Each copper centre presents a slightly distorted, square pyramidal coordination geometry (Addison's geometric index[40] $\tau_5 = 0.18$), with the central nitrogen atom of the macrocycle occupying the slightly elongated axial position of the complex ($d_{Cu\text{-}N}$ = 2.22 Å). The Cu pyridine bond presents the shortest distance ($d_{Cu\text{-}N}$ = 1.95 Å), closely followed by the Cu-O one, that can be identified as the connection between monomers ($d_{Cu\text{-}O}$ = 1.96 Å). Furthermore, **L1** adopts a bent conformation when coordinating copper: the angles defined by the planes of the pyridine ring and the one going through the polyamine nitrogen atoms are 104.60°.

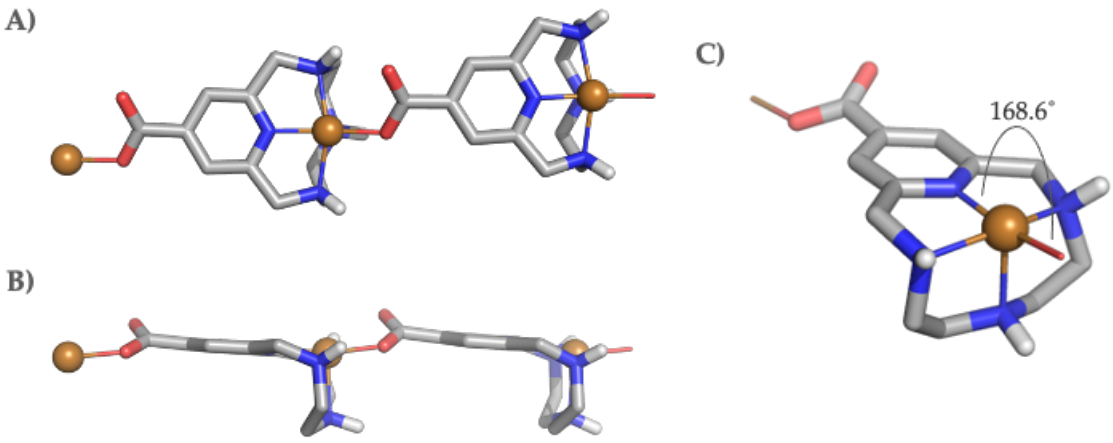

Figure S19. Structure of the concatenated $[Cu(H_{-1}L1)]^{+}$ complexes. Top (A), lateral (B) and oblique (C) perspectives of the chain; only polar hydrogens have been represented for simplification. CCDC id. 2060436.

It should be noted that, though polymeric have been characterized as crystalline samples of the complexes, such polynuclear compounds have not been observed in the experimental conditions used for the studies, nor are possible when the ligand is anchored onto the surface of the BNPs. As previously shown, only the mononuclear $[Cu(H_{-1}\mathbf{L1})]^{+}$ and $[Cu(H_{-1}\mathbf{L1})(OH)]$ species were identified by the potentiometric studies in aqueous media. High resolution mass spectroscopy supports the formation of only mononuclear species at the millimolar concentrations used in the solution studies. The spectra corresponding to both analysis can be found in Figures S20-S23.

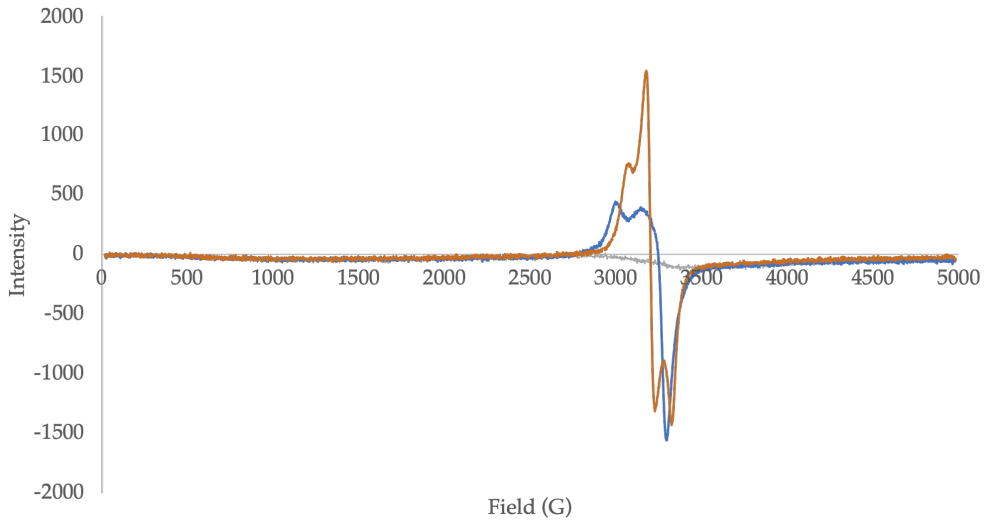

Figure S20. EPR measurement of a solution containing Cu(II):**L1** (blue line) or Cu(II):**L2** (orange) in 1:1 molar ratio. Baseline has been represented in grey.

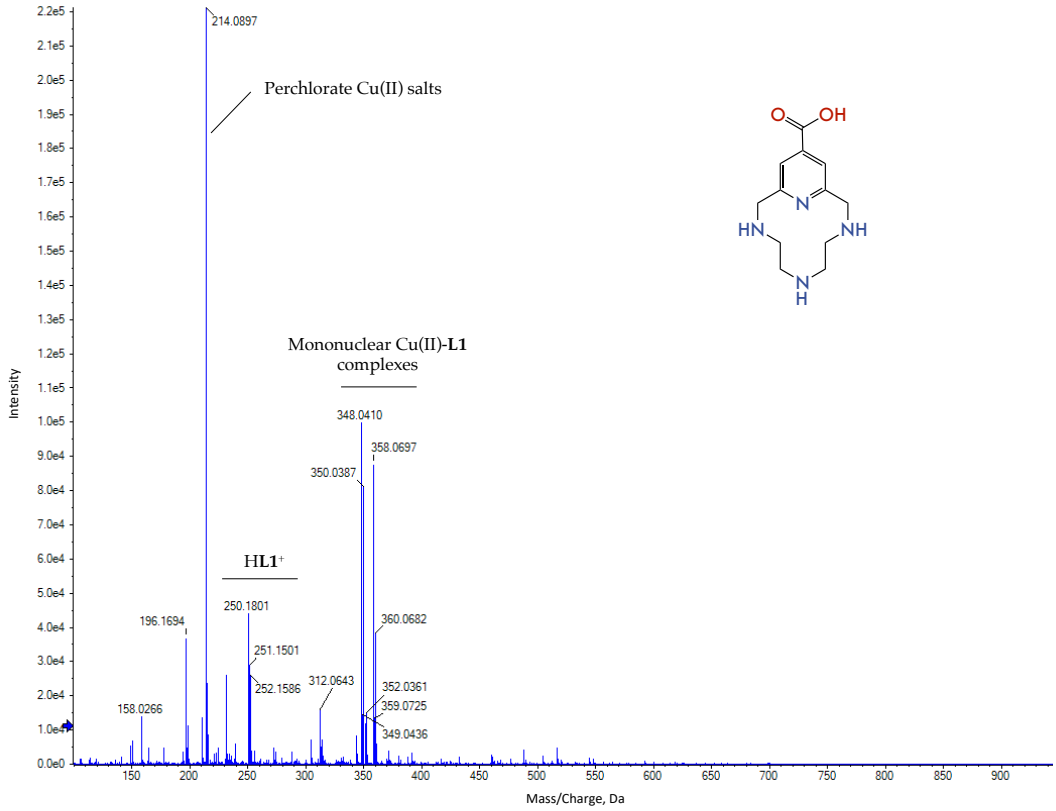

Figure S21. ESI-HR-MS of Cu^{2+}-**L1** in H_2O.

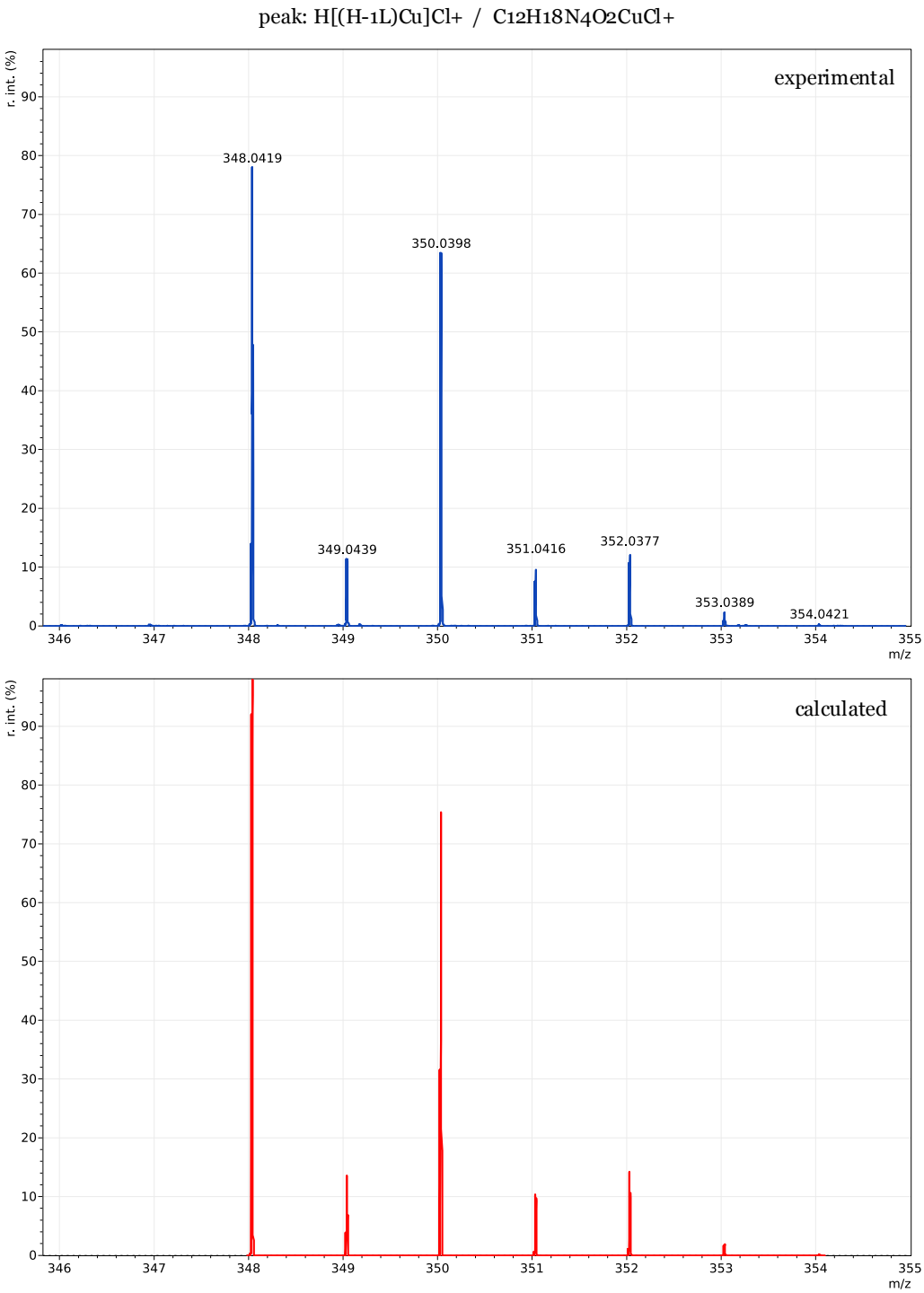

Figure S22. Detail of the ESI-HR-MS spectrum of Cu^{2+}-**L1** in H_2O at *ca.* 350 g mol^{-1}. Both the experimental (in blue) and the theoretical (in red) spectra have been represented.

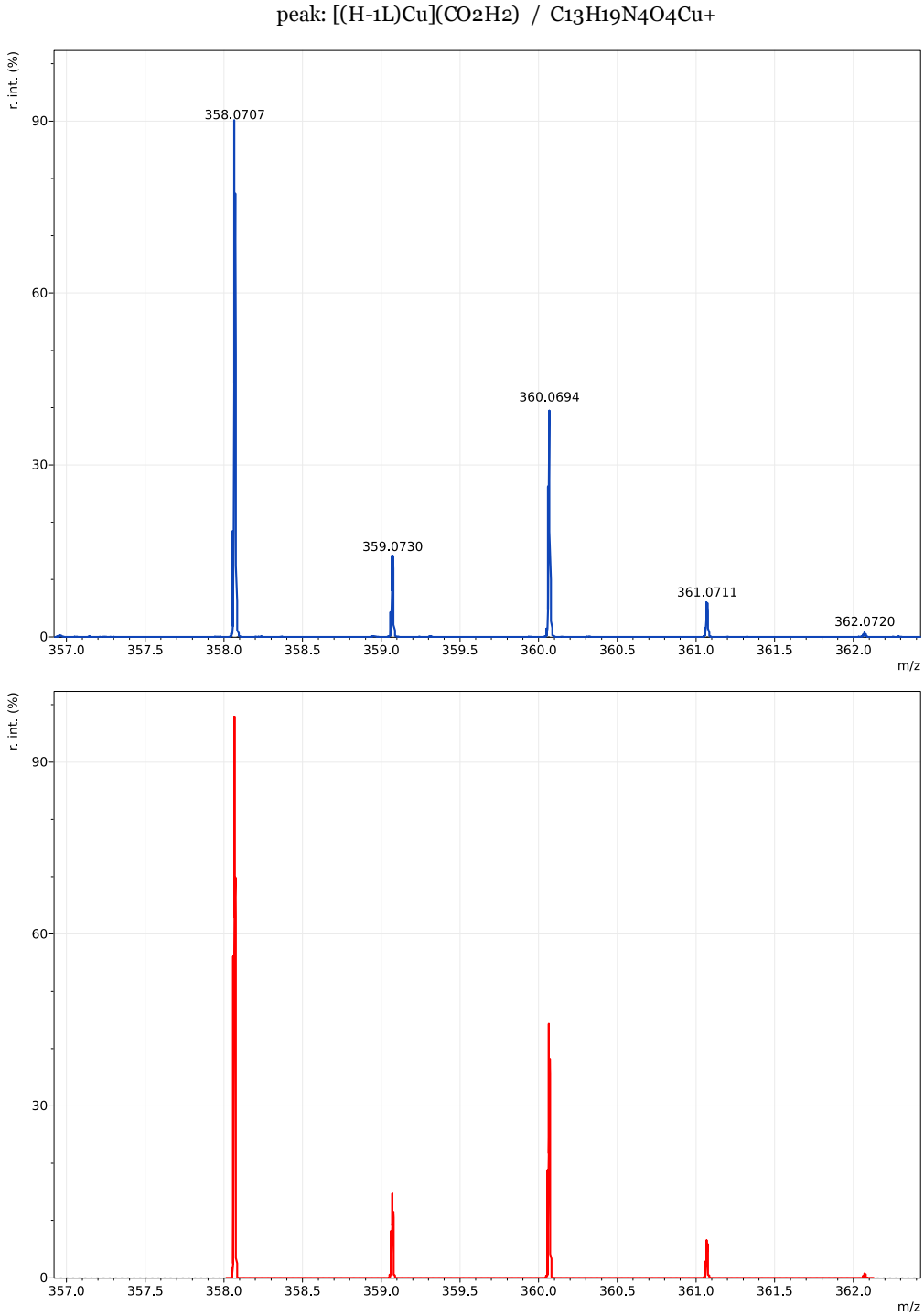

Figure S23. Detail of the ESI-HR-MS spectrum of Cu^{2+}-**L1** in H_2O at *ca.* 360 g mol^{-1}. Both the experimental (in blue) and the theoretical (in red) spectra have been represented.

IV. OTHER FIGURES

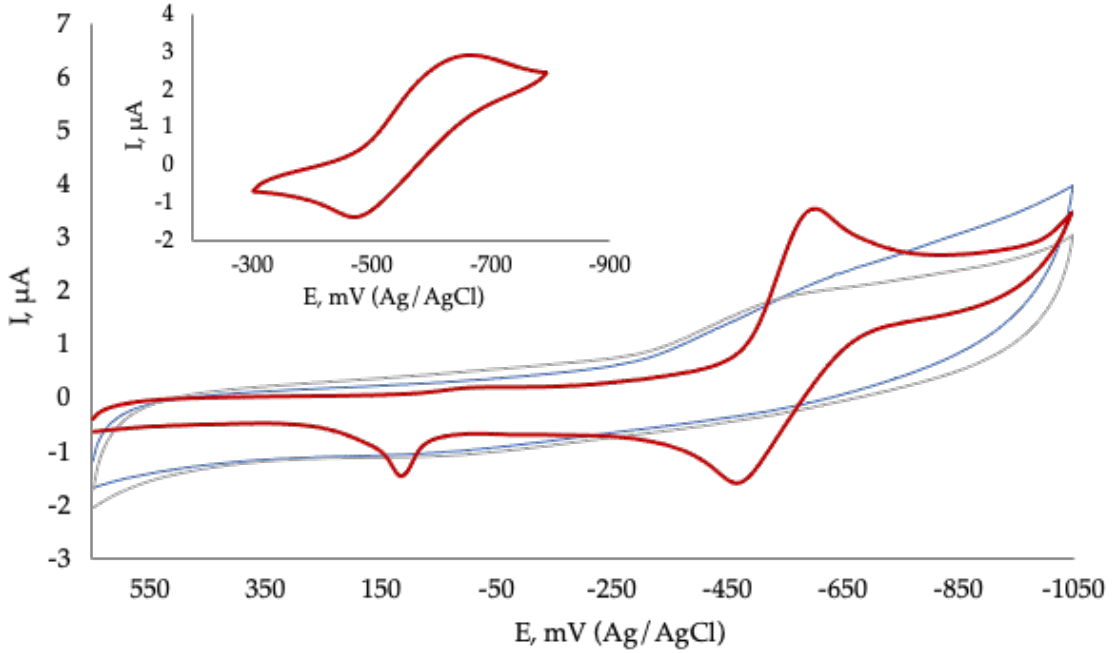

Figure S24. Cyclic voltammograms at the glassy carbon electrode of a 1.0 mM solution of Cu^{2+}-**L1** (red) in 50 mM TRIS buffer at pH 7.0. Potential scan initiated at 0.2 V in the positive direction. Potential scan rate 50 mV s^{-1}. In blue and grey have been represented, respectively, the blank samples of 50 mM TRIS buffer and a 1 mM solution of **L1**.

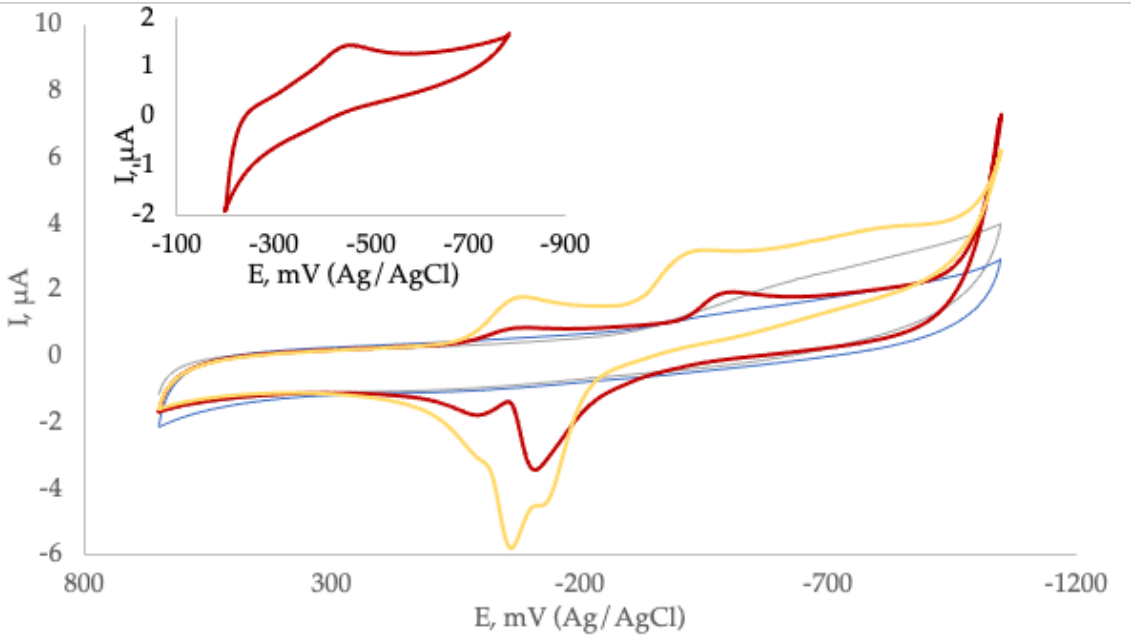

Figure S25. Cyclic voltammograms at the glassy carbon electrode of a 1.0 mM solution of Cu^{2+}-**BNPL1** (red) in 50 mM TRIS buffer at pH 7.0. Potential scan initiated at 0.2 V in the positive direction. Potential scan rate 50 mV s^{-1}. In blue, grey and yellow have been represented, respectively, the blank samples of 50 mM TRIS buffer, a 1 mM solution of **L1** and a 0.1 M solution of $Cu(ClO_4)_2$ in the same conditions.

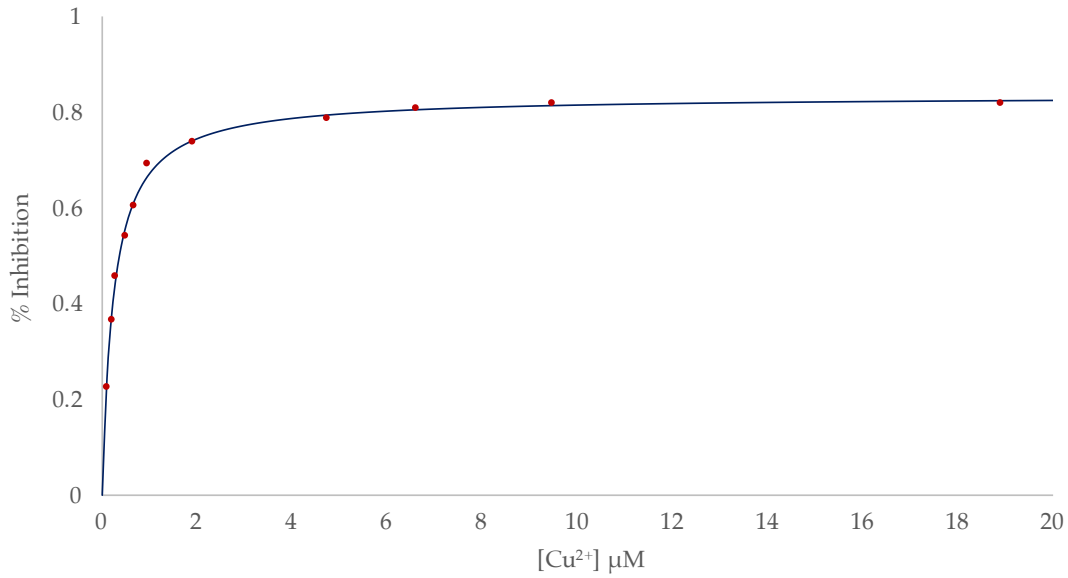

Figure S26. Fitting of the SOD activity data obtained by the McCord-Fridovich method for the system Cu-**L1**.

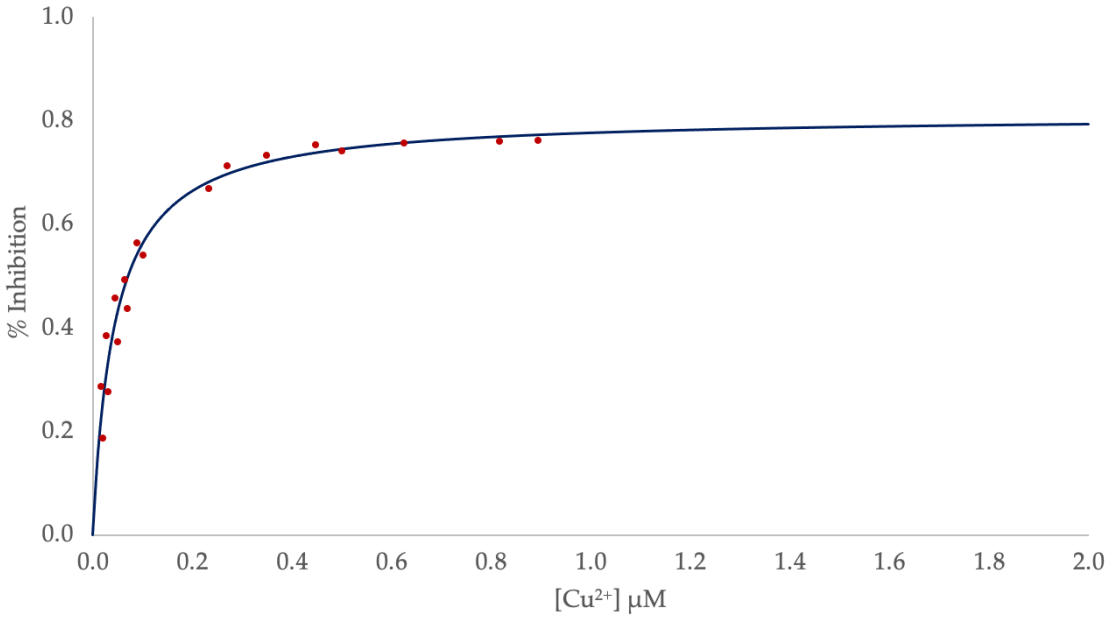

Figure S27. Fitting of the SOD activity data obtained by the McCord-Fridovich method for the system BNP-Cu-**L1**.

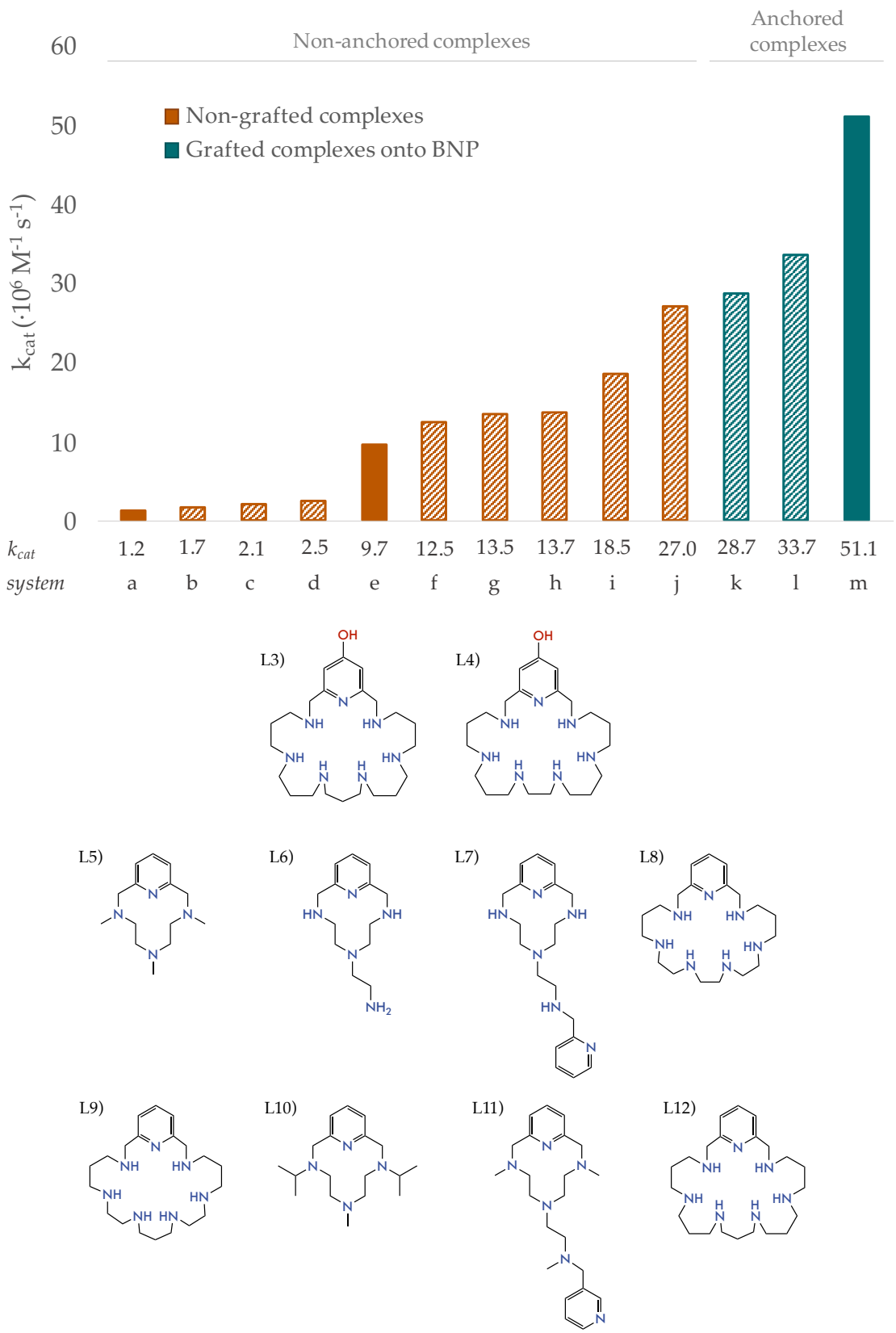

Figure S28. Representation of the catalytic constant values of the systems (a) Cu-**L5**,[1] (b) Cu-**L2**, (c) Cu-**L6**,[2] (d) Cu-**L7**,[2] (e) Cu-**L1**, (f) Cu_2-**L8**,[3] (g) Cu_2-**L9**,[3] (h) Cu-**L10**,[1] (i) Cu-**L11**,[2] (j) Cu_2-**L12**,[3] (k) Cu_2-**BNP-L3**,[4] (l) Cu_2-**BNP-L4**,[4] (m) Cu-**BNP-L1**.

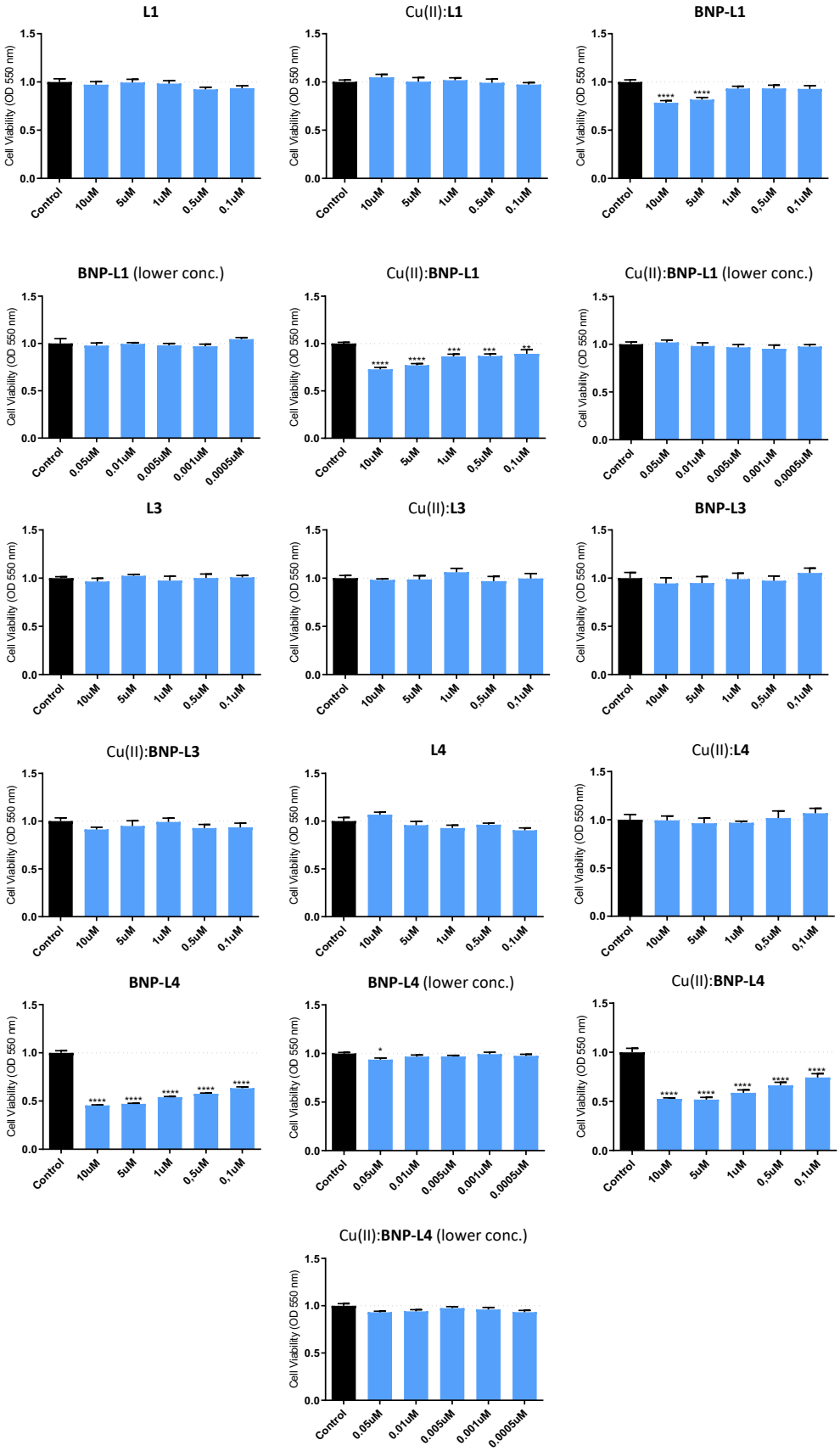

Figure S29. Representation of the cell viability of HEK293T cells in presence of different concentrations of the studied systems.

V. OTHER TABLES

Table S5. Evaluation of the SOD activity of the Cu^{2+} systems with **L1** and **L2**[1] at pH 7.4. The table shows the values of IC_{50} (defined as the amount of compound necessary for achieving 50% inhibition of NBT reduction to formazan by the superoxide anion) and k_{cat} of both the Cu^{2+}:**L1** and the Cu^{2+}:**BNP-L1** complexes.

System	IC_{50} (μM)	k_{cat} (10^6 M^{-1} s^{-1})
Cu^{2+}:**L1**	0.36(1)[a]	9.7
Cu^{2+}:**L2** [b]	2.1(4)	1.7
Cu^{2+}:**BNP-L1**	0.071(6)	51.1
$Cu(ClO_4)_2$[c]	1.1(1)	2.7
CuZn-SOD[c]	0.010(2)	430

[a]Values in parenthesis are standard deviations in the last significant figure.

[b] Taken from ref. [1].

[c] Taken from ref. [41].

REFERENCES

[1] Á. Martínez-Camarena, A. Liberato, E. Delgado-Pinar, A. G. Algarra, J. Pitarch-Jarque, J. M. Llinares, M. Á. Mañez, A. Domenech-Carbó, M. G. Basallote, E. García-España, *Inorg. Chem.* **2018**, *57*, 10961–10973.

[2] A. Nebot-Guinot, A. Liberato, M. A. Máñez, M. P. Clares, A. Doménech, J. Pitarch-Jarque, A. Martínez-Camarena, M. G. Basallote, E. García-España, *Inorganica Chim. Acta* **2018**, *472*, 139–148.

[3] R. Belda, S. Blasco, B. Verdejo, H. R. Jiménez, A. Doménech-Carbó, C. Soriano, J. Latorre, C. Terencio, E. García-España, *Dalton Trans.* **2013**, *42*, 11194–204.

[4] Á. Martínez-Camarena, J. M. Llinares, A. Domenech-Carbó, J. Alarcón, E. García-España, *RSC Adv.* **2019**, *9*, 41549–41560.

[5] E. Garcia-Espana, M. J. Ballester, F. Lloret, J. M. Moratal, J. Faus, A. Bianchi, *J. Chem. Soc. Dalt. Trans. Inorg. Chem.* **1988**, *2*, 101–104.

[6] M. Fontanelli, M. Micheloni, **1990**.

[7] G. Gran, *Analyst* **1952**, *77*, 661–671.

[8] F. J. C. Rossotti, H. Rossotti, *J. Chem. Educ.* **1965**, *42*, 375.

[9] P. Gans, A. Sabatini, A. Vacca, *Talanta* **1996**, *43*, 1739–1753.

[10] L. Alderighi, P. Gans, A. Ienco, D. Peters, A. Sabatini, A. Vacca, *Coord. Chem. Rev.* **1999**, *184*, 311–318.

[11] P. Gans, B. O'Sullivan, (VLpH (see: http://www.hyperquad.co.uk/vlph.htm), Unpublished).

[12] A. K. Covington, M. Paabo, R. A. Robinson, R. G. Bates, *Anal. Chem.* **1968**, *40*, 700–706.

[13] H. Hope, *Acta Crystallogr.* **1988**, *B44*, 22–26.

[14] Agilent, **2014**.

[15] G. M. Sheldrick, *Acta Crystallogr. Sect. A Found. Crystallogr.* **2015**, *71*, 3–8.

[16] O. V. Dolomanov, L. J. Bourhis, R. J. Gildea, J. A. K. Howard, H. Puschmann, *J. Appl. Crystallogr.* **2009**, *42*, 339–341.

[17] C. R. Groom, I. J. Bruno, M. P. Lightfoot, S. C. Ward, *Acta Crystallogr. Sect. B Struct. Sci. Cryst. Eng. Mater.* **2016**, *72*, 171–179.

[18] L. W. Oberley, D. R. Spitz, *Oxygen Radicals in Biological Systems*, Elsevier, **1984**.

[19] L. W. Oberley, D. R. Spitz, *Handbook of Methods of Oxygen Radicals Research*, CRC Press, Boca Raton, USA, **1986**.

[20] C. Beauchamp, I. Fridovich, *Anal. Biochem.* **1971**, *44*, 276–287.

[21] J. Y. Zhou, P. Prognon, *J. Pharm. Biomed. Anal.* **2006**, *40*, 1143–8.

[22] B. H. J. Bielski, H. W. Richter, *J. Am. Chem. Soc.* **1977**, *99*, 3019–3023.

[23] R. F. Pasternack, B. Halliwell, *J. Am. Chem. Soc.* **1979**, *101*, 1026–1031.

[24] S. Durot, C. Policar, F. Cisnetti, F. Lambert, J.-P. Renault, G. Pelosi, G. Blain, H. Korri-Youssoufi, J.-P. Mahy, *Eur. J. Inorg. Chem.* **2005**, *2005*, 3513–3523.

[25] S. Laurent, L. Vander Elst, C. Galaup, N. Leygue, S. Boutry, C. Picard, R. N. Muller, *Contrast Media Mol. Imaging* **2014**, *9*, 300–312.

[26] N. Leygue, A. Perez e Iñiguez De Heredia, C. Galaup, E. Benoist, L. Lamarque, C. Picard, *Tetrahedron* **2018**, *74*, 4272–4287.

[27] N. Leygue, M. Enel, A. Diallo, B. Mestre-Voegtlé, C. Galaup, C. Picard, *European J. Org. Chem.* **2019**, *2019*, 2899–2913.

[28] C. Féau, E. Klein, P. Kerth, L. Lebeau, *Bioorg. Med. Chem. Lett.* **2007**, *17*, 1499–1503.

[29] I. Lázár, *Synth. Commun.* **1995**, *25*, 3181–3185.

[30] R. Aucejo, P. Díaz, E. García-España, J. Alarcón, E. Delgado-Pinar, F. Torres, C. Soriano, M. C. Guillem, *New J. Chem.* **2007**, *31*, 44–51.

[31] Y. An, M. Chen, Q. Xue, W. Liu, *J. Colloid Interface Sci.* **2007**, *311*, 507–513.

[32] A. Ebrahiminezhad, Y. Ghasemi, S. Rasoul-Amini, J. Barar, S. Davaran, *Colloids Surfaces B Biointerfaces* **2013**, *102*, 534–539.

[33] J. E. Sarneski, H. L. Surprenant, F. K. Molen, C. N. Reilley, *Anal. Chem.* **1975**, *47*, 2116–2124.

[34] S. P. Dagnall, D. N. Hague, M. E. McAdam, *J. Chem. Soc. Perkin Trans. 2* **1984**, 435–440.

[35] S. P. Dagnall, D. N. Hague, M. E. McAdam, *J. Chem. Soc. Perkin Trans. 2* **1984**, 1111–1114.

[36] D. N. Hague, A. D. Moreton, *J. Chem. Soc. Perkin Trans. 2* **1994**, 265–270.

[37] C. Frassineti, S. Ghelli, P. Gans, A. Sabatini, M. S. Moruzzi, A. Vacca, *Anal. Biochem.* **1995**, *231*, 374–382.

[38] A. Bencini, A. Bianchi, E. Garcia-España, M. Micheloni, J. A. Ramirez, *Coord. Chem. Rev.* **1999**, *188*, 97–156.

[39] J. Costa, R. Delgado, *Inorg. Chem.* **1993**, *32*, 5257–5265.

[40] A. W. Addison, T. N. Rao, J. Reedijk, J. van Rijn, G. C. Verschoor, *J. Chem. Soc., Dalt. Trans.* **1984**, *251*, 1349–1356.

[41] H. Ohtsu, Y. Shimazaki, A. Odani, O. Yamauchi, W. Mori, S. Itoh, S. Fukuzumi, *J. Am. Chem. Soc.* **2000**, *122*, 5733–5741.